

# Online Research @ Cardiff

This is an Open Access document downloaded from ORCA, Cardiff University's institutional repository: <https://orca.cardiff.ac.uk/id/eprint/145323/>

This is the author's version of a work that was submitted to / accepted for publication.

Citation for final published version:

Gleeson, Matthew L. M., Gibson, Sally A. and Stock, Michael J. 2022. Constraints on the behaviour and content of volatiles in Galápagos magmas from melt inclusions and nominally anhydrous minerals. *Geochimica et Cosmochimica Acta* 319 , pp. 168-190. 10.1016/j.gca.2021.11.005 file

Publishers page: <https://doi.org/10.1016/j.gca.2021.11.005>  
<<https://doi.org/10.1016/j.gca.2021.11.005>>

Please note:

Changes made as a result of publishing processes such as copy-editing, formatting and page numbers may not be reflected in this version. For the definitive version of this publication, please refer to the published source. You are advised to consult the publisher's version if you wish to cite this paper.

This version is being made available in accordance with publisher policies.

See

<http://orca.cf.ac.uk/policies.html> for usage policies. Copyright and moral rights for publications made available in ORCA are retained by the copyright holders.



# 1 Constraints on the behaviour and content of 2 volatiles in Galápagos magmas from melt 3 inclusions and nominally anhydrous minerals

4 Matthew L. M. Gleeson<sup>1,2\*</sup>, Sally A. Gibson<sup>2</sup>, Michael J. Stock<sup>3</sup>, and EIMF<sup>4</sup>

5 <sup>1</sup>School of Earth and Environmental Sciences, Cardiff University, Main Building, Park Place, Cardiff,  
6 CF10 3AT, UK.

7 <sup>2</sup>Department of Earth Sciences, University of Cambridge, Downing Street, Cambridge, CB2 3EQ, UK.

8 <sup>3</sup>Department of Geology, Trinity College Dublin, College Green, Dublin 2, Ireland.

9 <sup>4</sup>Edinburgh Ion Microprobe Facility, University of Edinburgh, Grant Institute, School of Geosciences, Edinburgh,  
10 EH9 3FE, UK.

11 Corresponding author email address: gleesonm1@cardiff.ac.uk

## 12 ABSTRACT

---

13 Despite their relatively low concentration in most oceanic basalts, volatile species (e.g. H<sub>2</sub>O, CO<sub>2</sub> and  
14 S) have a disproportionately large influence on a wide range of mantle and magmatic processes.  
15 However, constraining the concentration of H<sub>2</sub>O (and other volatiles) in basaltic magmas is not  
16 straightforward as submarine glass analyses are influenced by assimilation of hydrothermal brines,  
17 and the melt inclusion record is often reset by post-entrapment processes. Nevertheless, in this  
18 study we show that it is possible to reconstruct a detailed history of the volatile content of basaltic  
19 magmas through integration of multiple discreet volatile records and careful consideration of  
20 secondary processes. We present new analyses of volatiles in olivine-hosted melt inclusions, melt  
21 embayments and nominally anhydrous minerals (NAMS, clinopyroxene and orthopyroxene) found in  
22 basalts erupted on Floreana Island in the south-eastern Galápagos Archipelago. Our results indicate  
23 that the Floreana magmas, which are characterised by the most radiogenic Pb and Sr isotope  
24 signatures in the Galápagos Archipelago, contain H<sub>2</sub>O concentrations between 0.4 and 0.8 wt% (at a  
25 melt Mg# of 0.65, where Mg# = Mg/(Mg + Fe) molar). These are marginally greater than the H<sub>2</sub>O  
26 contents of magmas beneath Fernandina in the western Galápagos Archipelago (cf. 0.2–0.7 wt% H<sub>2</sub>O  
27 at Mg# = 0.65). While the volatile content of magmas from the western archipelago follow trends

28 defined by concurrent mixing and crystallisation, NAMs from Floreana reveal the presence of rare,  
29 volatile-rich magmas (~2 wt% H<sub>2</sub>O) that form as a consequence of reactive porous flow in mush-  
30 dominated magmatic systems beneath the south-eastern Galápagos. Furthermore, the Floreana  
31 magmas have similar H<sub>2</sub>O/light Rare Earth Element ratios to basalts from the western Galápagos but  
32 contain F/Nd and Cl/K ratios that are ~2 – 3 times greater, indicating that the mantle source of the  
33 Floreana lavas might represent an important halogen reservoir in the Galápagos mantle plume.

## 34 1 INTRODUCTION

---

35 Magmatic volatiles (e.g. H<sub>2</sub>O, CO<sub>2</sub> and S) have a major impact on mantle melting and rheology,  
36 crustal magma processing, and the timing and style of volcanic eruptions (Asimow et al., 2004;  
37 Asimow and Langmuir, 2003; Gaetani and Grove, 1998; Hirth and Kohlstedt, 2003, 1996; Stock et al.,  
38 2016). To advance understanding of magma system dynamics and mantle processes it is essential to  
39 place robust constraints on the volatile concentrations of magmas and their mantle source regions,  
40 as well as the behaviour of volatile species during magma ascent and eruption. In addition, in ocean  
41 island settings magmas are derived from melting in deep-sourced mantle plumes and deconvolving  
42 their volatile record offers a unique opportunity to study the volatile composition of recycled and  
43 primordial material stored in the Earth's lower mantle (Hofmann, 1997; White, 2010; Zindler and  
44 Hart, 1986).

45 Determining the pre-eruptive volatile content of silicate melts is complicated by the low-solubility of  
46 these components at low pressures (Dixon, 1997; Ghiorso and Gualda, 2015; Shishkina et al., 2014),  
47 which results in magma degassing during crustal storage, magma ascent, and cooling at the surface.  
48 The influence of low-pressure degassing on the H<sub>2</sub>O and S contents of silicate melts can be mitigated  
49 by analysing the glassy exteriors of lava flows that are erupted under 100s to 1000s of metres of  
50 water, as the pressure of the overlying water column prevents significant loss of H<sub>2</sub>O and S to the  
51 vapour phase (Dixon, 1997; Jackson et al., 2015; Peterson et al., 2017; Shimizu et al., 2016).

52 However, the volatile record preserved in submarine glasses is frequently complicated by post-  
53 eruptive hydration (Friedman and Long, 1976) and assimilation of Cl-rich brines during shallow  
54 magma storage and/or ascent (Kendrick et al., 2015; Le Roux et al., 2006). Consequently, many  
55 studies have instead focused on the use of melt inclusions to constrain magma volatile systematics  
56 (e.g. Cabral et al., 2014; Hartley et al., 2015; Koleszar et al., 2009; Métrich et al., 2014; Miller et al.,  
57 2019; Saal et al., 2002; Wieser et al., 2020). In theory, pockets of melt that are trapped within  
58 crystals are less likely to be affected by assimilation of Cl-rich components and might act as pressure  
59 vessels during magma ascent, inhibiting volatile degassing into a vapour phase (Lowenstern, 1995).  
60 Nevertheless, melt inclusions rarely provide a uncompromised record of magmatic H<sub>2</sub>O or CO<sub>2</sub> at the  
61 time of entrapment -- due to the influence of decrepitation, post entrapment crystallisation,  
62 migration of volatile species into a vapour bubble and the geologically-fast diffusion of volatile  
63 species (primarily H<sub>2</sub>O) through common crystal hosts, (Gaetani et al., 2012; Hartley et al., 2015;  
64 Maclennan, 2017; Steele-Macinnis et al., 2011). If secondary processes are carefully considered,  
65 however, melt inclusions and submarine glasses can still be used to evaluate magmatic volatile  
66 records.

67 To address the limitations of melt inclusion and submarine glass analyses, several studies have  
68 recently investigated the use of alternative methods for constraining magmatic volatile contents. For  
69 example, nominally anhydrous minerals (NAMs) incorporate volatiles as trace components, which  
70 can be related to the volatile contents of co-existing melts if the relevant Nernstian partition  
71 coefficients are known (Edmonds et al., 2016; Lloyd et al., 2016; Nazzareni et al., 2020; O'Leary et al.,  
72 2010; Turner et al., 2017; Wade et al., 2008). In addition, clinopyroxene crystals are less susceptible  
73 to low-pressure diffusive loss of H<sub>2</sub>O than olivine-hosted melt inclusions (due to slower H<sub>2</sub>O  
74 diffusivities; Costa et al., 2020; Ferriss et al., 2016; Turner et al., 2017), and might provide a more  
75 reliable record of pre-eruptive magma volatile contents. However, as erupted magmas often contain  
76 inherited (e.g. xenocrystic or antecrystic) material that did not form directly from their carrier liquid

77 (Gleeson et al., 2020a; Ubide et al., 2014; Wieser et al., 2019), detailed petrological characterisation  
78 is required to understand the relationship between the erupted crystal cargo and carrier melt before  
79 NAMs can be reliably interpreted to understand pre-eruptive magmatic volatiles.

80 In this study, we integrate published data from submarine glasses and melt inclusions with new  
81 analyses of melt inclusions, melt embayments (defined here as melt pockets that are partially  
82 enclosed by a host olivine crystal) and NAMs to: (i) determine the pre-eruptive concentration of  
83 volatile components such as H<sub>2</sub>O and CO<sub>2</sub> for two well characterised regions of the Galápagos  
84 Archipelago that display highly contrasting eruptive styles (Floreana in the south-eastern archipelago  
85 and Fernandina in the western archipelago; Fig. 1; Allan and Simkin, 2000; Gleeson et al., 2020a;  
86 Harpp et al., 2014; Harpp and White, 2001; Koleszar et al., 2009; Peterson et al., 2017); (ii) identify  
87 how the volatile contents of each system evolve during magmatic differentiation; and (iii) place  
88 improved constraints on the volatile content of the Galápagos mantle plume. By combining these  
89 datasets and carefully considering the impact of secondary processes, we obtain a more  
90 comprehensive picture of the sub-volcanic volatile systematics than would be possible using any  
91 single petrological volatile record in isolation. In addition, our new data enable us to determine the  
92 impact of different mantle components on the volatile budget of ascending ocean island basalts  
93 (OIBs).

## 94 2 GEOLOGICAL SETTING

---

### 95 2.1 GEOCHEMICAL HETEROGENEITY IN THE GALÁPAGOS PLUME

96 The Galápagos mantle plume displays complex spatial heterogeneity in its trace element, isotopic  
97 and lithological composition (Geist et al., 1988; Gleeson et al., 2021; Gleeson et al., 2020b; Harpp  
98 and White, 2001; Hoernle et al., 2000; White et al., 1993). A minimum of 4 isotopic components  
99 intrinsic to the Galápagos plume are expressed in the geochemistry of erupted basalts across the  
100 archipelago, with at least three isotopically enriched mantle components (referred to as the PLUME

101 – high  $^3\text{He}/^4\text{He}$ ; FLO – high  $^{206}\text{Pb}/^{204}\text{Pb}$ ; and WD – high  $^{207}\text{Pb}/^{206}\text{Pb}$  - components) identified in  
102 addition to an isotopically depleted eastern component (Harpp and White, 2001; Hoernle et al.,  
103 2000; White et al., 1993; Fig. 1). However, the simple spatial pattern of mantle heterogeneity in the  
104 Galápagos plume that has been identified through analyses of radiogenic isotope ratios, where  
105 enriched isotopic signatures are predominantly found in basalts from the southern and western  
106 Galápagos and isotopically depleted signatures are observed in the eastern Galápagos (Harpp and  
107 Weis, 2020), is complicated by the non-trivial relationship between isotopic and lithological  
108 heterogeneity (i.e., the presence of pyroxene-rich, and thus more fusible components in the  
109 Galápagos mantle plume; Gleeson and Gibson, 2019; Vidito et al., 2013). In fact, it has recently been  
110 proposed that a ‘central pyroxenite’ component is present in the mantle source region of volcanoes  
111 in the northern and central Galápagos, separating isotopically enriched signatures to the south-west  
112 from isotopically depleted signatures in the north-east (Gleeson et al., 2021).

113 The Floreana basalts have slightly elevated He isotope ratios ( $\sim 11 R/R_A$ ) compared to mid-ocean  
114 ridge basalts (MORBs;  $\sim 8 R/R_A$ ) and radiogenic Sr and Pb isotope signatures relative to basalts  
115 erupted in other regions of the Galápagos Archipelago ( $^{206}\text{Pb}/^{204}\text{Pb} \sim 19.55\text{--}20.06$  and  $^{87}\text{Sr}/^{86}\text{Sr}$   
116  $\sim 0.70325\text{--}0.70359$ ; Harpp et al., 2014; Harpp and White, 2001; Kurz and Geist, 1999). They are also  
117 characterised by high light-to-middle rare earth element (REE) ratios, but low middle-to-heavy REE  
118 ratios, resulting in a notable concave up REE signature (Harpp et al., 2014). In contrast to Floreana,  
119 basalts erupted on or near Fernandina typically have unradiogenic He and Ne isotope signatures  
120 ( $^3\text{He}/^4\text{He} \sim 29 R/R_A$ ;  $^{20}\text{Ne}/^{22}\text{Ne} \sim 12.5$  at  $^{21}\text{Ne}/^{22}\text{Ne} \sim 0.034$ ; Kurz et al., 2009) and moderately  
121 radiogenic Sr and Pb isotope signatures ( $^{206}\text{Pb}/^{204}\text{Pb} \sim 19.10$  and  $^{87}\text{Sr}/^{86}\text{Sr} \sim 0.70325$ ; Harpp and White,  
122 2001; Peterson et al., 2017; Saal et al., 2007).

## 123 2.2 VARIATIONS IN MELT FLUX, GEOMORPHOLOGY AND ERUPTIVE STYLES

124 The islands of Fernandina and Floreana are characterised by contrasting volcanic morphologies and  
125 eruptive styles (Allan and Simkin, 2000; Bow and Geist, 1992; Harpp et al., 2014; Harpp and Geist,

126 2018; Lyons et al., 2007). Fernandina is located near the centre of the postulated Galápagos plume  
127 stem, whereas Floreana is ~100 km downstream (i.e. in the direction of Nazca plate motion; Fig. 1;  
128 Hooft et al., 2003; Villagómez et al., 2014). As a result, the flux of magma into the lithosphere  
129 beneath Fernandina is substantially greater than beneath Floreana, which is manifest in a volumetric  
130 eruption rate at least six orders of magnitude greater at Fernandina (Harpp et al., 2014; Poland,  
131 2014).

132 Unlike other Galápagos islands, Floreana magmas are predominantly stored in the lithospheric  
133 mantle (at ~24 km depth; Gleeson et al., 2020a). Additionally, there is a high proportion of  
134 pyroclastic material on Floreana (relative to the volume of effusive lavas) compared to the other  
135 Galápagos islands, and the deposits contain an unusual abundance of mafic and ultramafic xenoliths  
136 (Harpp et al., 2014; Lyons et al., 2007). These features have been interpreted as evidence for rapid  
137 magma ascent rates, which might result from high volatile concentrations in Floreana primary melts  
138 (Harpp et al., 2014). However, while this hypothesis is consistent with many of the volcanological  
139 features on Floreana, no analytical constraints currently exist on the volatile contents of magmas  
140 beneath the island.

141 The comparatively high flux of magma into the lithosphere beneath Fernandina has resulted in  
142 development of a magmatic storage region in the mid- to lower-crust, which is characterised by both  
143 crystal-rich and melt-rich regions, and the formation of a single volcanic edifice with a large central  
144 caldera (Allan and Simkin, 2000; Geist et al., 2014, 2006). Although localized, small, compositionally  
145 diverse melts have been evidenced in the crust (i.e., the presence of melts of andesitic – dacitic  
146 compositions), the high flux of magma into the Fernandina sub-volcanic system efficiently buffers  
147 the mean composition of erupted magmas (Geist et al., 2014; Stock et al., 2020). Both subaerial and  
148 submarine eruptions on Fernandina are typically effusive, with basaltic lava flows originating from  
149 either circumferential or radial fissures (Chadwick et al., 2011; Vasconez et al., 2018).

## 150 3 METHODOLOGY

---

### 151 3.1 SAMPLES AND PREPARATION

152 Melt inclusions, embayments, matrix glass and nominally anhydrous minerals (clinopyroxene and  
153 orthopyroxene) were analysed from a single sample (17MMSG16) of fresh scoria lapilli (total volume  
154 of  $\sim 200\text{--}500\text{ cm}^3$ , individual scoria fragments typically 0.5–1.5 cm diameter) that was collected from  
155 the base of an emergent scoria cone on the northern coast of Floreana (Punta Cormorant;  
156  $90.42752^\circ\text{W}$ ,  $1.22495^\circ\text{S}$ ; Fig. 1). The scoria is olivine phyric with minor clinopyroxene ( $<5\text{ vol\%}$  of  
157 crystals) and very rare orthopyroxene ( $\ll 1\text{ vol\%}$ ). Clinopyroxene crystals were also analysed from 3  
158 wehrlite, 2 dunite, and 2 gabbroic xenoliths (2–10 cm across), collected from scoria cones on the  
159 northeast coast of Floreana (Fig. 1). Prior to geochemical analysis, the scoria and xenolith samples  
160 were crushed, and crystals hand-picked from the 0.25–0.5 and 0.5–1 mm size fractions.

161 Olivine-hosted melt inclusions are very rare in the Floreana scoria and are typically found in small  
162 crystals (0.25–0.5 mm long axis). Where present, there are often multiple inclusions or embayments  
163 in a single host crystal, which have been quenched on eruption. Although most melt inclusions are  
164 smaller ( $<10\text{ }\mu\text{m}$ ) than the beam size ( $\sim 20\text{ }\mu\text{m}$ ) used during secondary ion mass spectrometry (SIMS),  
165 the largest inclusions are analysable, extending to  $\sim 20\text{--}50\text{ }\mu\text{m}$  diameter (Fig. 2). Olivine crystals that  
166 contain melt inclusions and/or embayments were mounted individually in CrystalBond™ and hand  
167 polished until the glass was exposed at the surface. Once the melt inclusions and embayments were  
168 exposed, the crystals were removed from the CrystalBond™, mounted in epoxy resin and a final  
169 polish was applied. Clinopyroxene and orthopyroxene crystals that were separated from the  
170 Floreana scoria or xenoliths for NAM analyses were also mounted individually in CrystalBond™ and  
171 hand polished. After polishing, clinopyroxene and orthopyroxene crystals were removed from the  
172 CrystalBond™ and hand pressed into indium metal (at  $\sim 120^\circ\text{C}$  to soften the metal). The mounts  
173 were then flattened using a hydraulic press to ensure a flat sample surface for analysis.



174 Prior to Secondary Ion Mass Spectrometry (SIMS) and Electron Probe Microanalysis (EPMA),  
175 Backscatter Electron maps were created for all sample mounts, and images were taken of individual  
176 crystals, using a Field Emission Gun Scanning Electron Microscope (Quanta-650F) at the University of  
177 Cambridge (Fig. 2). Mapping was carried out in low vacuum mode (as samples were uncoated) using  
178 a ~5 nA beam current and a 20 kV accelerating voltage. To mitigate the risk of electron-beam  
179 induced sample damage (Humphreys et al., 2006) or contamination from C coating, volatiles (CO<sub>2</sub>,  
180 H<sub>2</sub>O, F, and Cl) were analysed in the Floreana glasses and NAMs by SIMS prior to exposure to a  
181 focused electron beam (EPMA).

### 182 3.2 SECONDARY ION MASS SPECTROMETRY (SIMS)

183 All glass (that is, matrix glasses, melt inclusions and melt embayments) and NAM samples were Au  
184 coated and analysed using a Cameca ims-4f instrument at the Edinburgh Ion Microprobe Facility  
185 (EIMF; University of Edinburgh). The NAM sample mounts were loaded into the instrument vacuum  
186 chamber and pumped down for 3 days prior to analysis to reduce H<sub>2</sub>O background count rates. All  
187 analyses were performed with a 14.5 keV <sup>16</sup>O<sup>-</sup> primary beam and a positive secondary ion beam. A  
188 liquid N<sub>2</sub> cold trap was attached to reduce background <sup>1</sup>H counts.

189 Glass volatile and trace element concentrations were measured using two separate SIMS protocols.  
190 Carbon was analysed first, using a 5 nA primary ion beam at high mass resolution (~1200 M/ΔM) to  
191 avoid <sup>24</sup>Mg<sup>2+</sup> interference, a 3 min pre-sputter rastering over a 30 μm<sup>2</sup> area, and a secondary ion  
192 energy filter of 50 ±25 V. <sup>12</sup>C backgrounds were determined via regular analysis of the host olivines  
193 and were between 1 and 4 cps (counts per second), which was subtracted from each analysis prior  
194 to calculation of sample CO<sub>2</sub> concentrations. Water, F, Cl and other trace elements were measured  
195 in a second analysis of the same spot at lower mass resolution (~300 M/ΔM), using a 5 nA primary  
196 beam, an energy offset of 75 ±25 V, and a ~2 min pre-sputter with a 30 μm<sup>2</sup> raster area. <sup>1</sup>H  
197 backgrounds were determined through analysis of olivine crystals that host melt inclusions and/or  
198 embayments. Background measurements were carried out several times during the analytical

199 session and were typically between 1100 and 1700 cps (corresponding to apparent H<sub>2</sub>O  
200 concentrations between 0.05 and 0.07 wt%). The background count rate was subtracted from the  
201 measured cps of each analysis prior to calculation of the measured H<sub>2</sub>O concentration. As the  
202 Floreana olivines are expected to contain only 10-20 ppm H<sub>2</sub>O (calculated using the partition  
203 coefficients for water ( $D^{\text{H}_2\text{O}}_{\text{olivine-melt}}$ ) of Hauri et al. (2006) and the measured concentration of H<sub>2</sub>O in  
204 the olivine-hosted melt inclusions), these background measurements are uninfluenced by the trace  
205 amounts of H<sub>2</sub>O that may be held in the olivine structure.

206 Nominally anhydrous mineral H<sub>2</sub>O concentrations were measured using a 5 nA primary beam, with a  
207 6 min pre-sputter rastered over 30  $\mu\text{m}^2$  to remove any H<sub>2</sub>O adsorbed onto the sample surface.  
208 Alongside <sup>1</sup>H, the isotopes <sup>19</sup>F, <sup>26</sup>Mg, <sup>27</sup>Al, <sup>30</sup>Si, <sup>35</sup>Cl, <sup>39</sup>K, <sup>44</sup>Ca and <sup>47</sup>Ti were also measured and were  
209 used to detect whether any standard analyses differed from their published values. Only high-energy  
210 secondary ions with an energy of 75  $\pm$ 25V were allowed in the mass spectrometer. An effective field  
211 aperture of 8  $\mu\text{m}$  was used to further reduce <sup>1</sup>H backgrounds. <sup>1</sup>H backgrounds were evaluated using  
212 the reference material CPX SMC31139 (Kumamoto et al., 2017), which contains 5 ppm H<sub>2</sub>O, as well  
213 as an olivine separated from the scoria of sample 17MMSG16. Repeat analyses of CPX SMC31139  
214 indicates that the <sup>1</sup>H backgrounds are between 1 and 7 cps (equivalent to 2-15 ppm H<sub>2</sub>O). Notably,  
215 these low background count rates indicate that the olivine of sample 17MMSG16 has 12 $\pm$ 2 ppm H<sub>2</sub>O  
216 ( $n=4$ ), consistent with the H<sub>2</sub>O contents estimated based on our melt inclusions analysis for sample  
217 17MMSG16 and published values of  $D^{\text{H}_2\text{O}}_{\text{olivine-melt}}$  (Hauri et al., 2006).

218 Laser Ablation Inductively Coupled Plasma Mass Spectrometry (LA-ICP-MS) analysis of the trace  
219 element composition of the clinopyroxene crystals analysed in this study were presented in Gleeson  
220 et al. (2020a). The LA-ICP-MS analyses were located directly on top of the much smaller SIMS pits.

221 For glasses, H<sub>2</sub>O and CO<sub>2</sub> concentrations were calculated from working curves of <sup>1</sup>H/<sup>30</sup>Si and  
222 <sup>12</sup>C/<sup>30</sup>Si\*SiO<sub>2</sub> produced using well-characterised basaltic glass standards (N72, M40, M10, and M36;  
223 Shishkina et al., 2010). Fluorine was calibrated against BCR-2g, whereas Cl and the other trace

224 elements were calibrated against GSD-1G (Marks et al., 2017), with  $^{30}\text{Si}$  as an internal standard.  
225 Middle REE and heavy REE were corrected for light REE $^{16}\text{O}$  or BaO interferences using  
226 predetermined oxide production rates, whereas  $^{85}\text{Rb}$  was corrected for  $^{56}\text{Fe}^{29}\text{Si}$  calculated from  
227  $^{56}\text{Fe}^{28}\text{Si}$  measured on mass 84 (after correcting for isobaric  $^{84}\text{Sr}$ ) using in-house ION6 software.  
228 Clinopyroxene volatile contents are underestimated when they are calculated from basaltic glass  
229  $^1\text{H}/^{30}\text{Si}$  working curves, due to different ion beam sputtering rates in the different matrices (i.e.  
230 matrix effects; Kumamoto et al., 2017; Supplementary Information). Consequently, the  $\text{H}_2\text{O}$  analyses  
231 were calibrated using recently-characterised clinopyroxene and orthopyroxene standards (only  
232 analyses that returned major element concentrations similar to the published values were used in  
233 the calibration slope; Kumamoto et al., 2017; Supplementary Information). Standards were analysed  
234 at regular intervals to check for instrument drift and to maintain the best-possible calibrations.  
235 The precision of SIMS analyses were tracked through repeat analysis of a microlite-free basaltic glass  
236 from Wolf volcano (Galápagos; sample 17MMSG39 of Stock et al., 2018) for  $\text{H}_2\text{O}$ , F, and Cl, standard  
237 material M40 (Shishkina et al., 2010) for  $\text{CO}_2$  and BCR-2g for other trace elements. Typical  $2\sigma$   
238 precision is  $\sim 10\%$ ,  $\sim 4\%$ ,  $\sim 7\%$  and  $\sim 5\%$  for  $\text{H}_2\text{O}$ , F, Cl and  $\text{CO}_2$ , respectively, and  $\sim 4\text{--}6\%$  for other trace  
239 elements, except Nd ( $\sim 10\%$ ) and the heavy REE (Tm, Yb, Lu;  $<20\%$ ). The  $2\sigma$  precision of NAM  $\text{H}_2\text{O}$   
240 analyses were determined through repeat analysis of homogeneous clinopyroxene cores from  
241 Floreana sample 17MMSG16 ( $\sim 10\%$ ) and repeat analysis of secondary standard materials (e.g. ALV-  
242 519-4-1;  $\sim 8\%$ ). Analytical recovery was determined through repeat analysis of a clinopyroxene  
243 standard (CPX-KH04-4; 90–105%, with an average recovery value of 100%; Kumamoto et al., 2017).

### 244 3.3 ELECTRON PROBE MICROANALYSIS (EPMA)

245 Following SIMS analysis, the samples were briefly re-polished (to remove the Au coat) and C coated.  
246 Glasses and clinopyroxenes were analysed for major ( $>1$  wt%) and minor elements ( $<1$  wt%) using a  
247 Cameca SX100 electron microprobe in the Department of Earth Sciences, University of Cambridge.  
248 Analytical routines and standard data for clinopyroxene and orthopyroxene analyses are reported in

249 Gleeson et al. (2020a) where EPMA spots were located as close as possible to the SIMS pits. For glass  
250 analyses, spots were also placed close to the SIMS pits and the EPMA was calibrated with  
251 appropriate mineral and metal standards (see Gleeson and Gibson, 2019 for details). Glass analyses  
252 were collected using a 6 nA, 15 kV, defocused (5  $\mu\text{m}$ ) beam. Sodium and K were analysed first (10s  
253 peak count time) to avoid alkali migration during electron beam exposure. Other elements were  
254 analysed with peak count times of 10s (Si), 20s (Fe), 30s (Al, P, Ca, Mg), 40s (Mn), or 60s (Ti);  
255 backgrounds were determined by counting for half the peak count time on either side of the peak).  
256 Sulphur was analysed last using a 20 nA beam and a 60s peak count time.

257 Analytical uncertainties were tracked through analysis of the VG2 standard material (Jarosewich et  
258 al., 1980). Typical  $2\sigma$  precision is <3% for major elements and <5-10% for minor elements. Analytical  
259 recovery was also measured through repeat analysis of VG2 (Jarosewich et al., 1980) and is typically  
260 98–102% for all elements.

## 261 **4 RESULTS**

---

### 262 **4.1 MELT INCLUSIONS, EMBAYMENTS AND MATRIX GLASSES**

263 In total, 25 olivine-hosted melt inclusions and embayments, and 13 matrix glasses were analysed  
264 from sample 17MMSG16 (Supplementary Data). A high proportion of olivine crystals in 17MMSG16  
265 are xenocrystic and no melt inclusions or embayments were identified in these crystals; all melt  
266 inclusion analyses in this study are from the autocrystic crystal population identified by Gleeson et  
267 al. (2020a), which is characterised by relatively high Ca contents in the olivine (>1500 ppm).

#### 268 **4.1.1 Major and trace elements**

269 The basaltic glasses analysed in this study typically plot above the alkali-tholeiite divide on a total  
270 alkali versus silica plot, straddling the transition between basalts and trachy-basalts (Fig. 3; Irvine  
271 and Baragar, 1971). They have higher total alkali contents ( $\text{Na}_2\text{O} + \text{K}_2\text{O} \sim 4\text{--}6 \text{ wt}\%$ ) than the Floreana  
272 whole-rock data (Harpp et al., 2014), but are comparable to previously-published matrix glass

273 analyses (Gleeson et al., 2020a). The melt inclusions and embayments have a similar range of  $\text{FeO}_t$   
274 contents to the Floreana whole-rock ( $\sim 8 - 10.5$  wt%) and are in Mg-Fe disequilibrium with their  
275 olivine hosts (i.e., melt inclusion glass Mg#, where  $\text{Mg\#} = \text{Mg}/(\text{Mg} + \text{Fe}_t)$  molar, are typically lower  
276 than expected based on the composition of the host olivines; Supplementary Information). As the  
277 similar range of melt inclusions and whole-rock  $\text{FeO}_t$  contents indicates that there is no clear Fe-loss  
278 during Post-Entrapment Crystallisation (PEC), we estimate the extent of PEC by adding back in the  
279 host olivine composition to each melt inclusion until olivine-melt equilibrium is achieved (assuming a  
280  $K_d$  of 0.30 and a  $\text{Fe}^{3+}/\text{Fe}_{\text{tot}}$  ratio of 0.15; Roeder and Emslie, 1970). These calculations indicate that  
281 each of the Floreana melt inclusions has undergone  $<10\%$  PEC. However, the large uncertainty in the  
282  $\text{FeO}_t$  content of the original trapped Floreana melts ( $8 - 10.5$  wt%  $\text{FeO}_t$ ), precludes accurate  
283 corrections for the chemical changes that occur during PEC (cf. Wieser et al., 2020). As a result, we  
284 use the measured melt inclusion compositions rather than the PEC corrected compositions in the  
285 following discussions.

286 The analysed glasses from Floreana are characterised by high concentrations of fluid mobile trace  
287 elements (e.g. Rb, Ba, K; Fig. 4) and moderately high concentrations of high field-strength elements  
288 (e.g. Ti, Ta, Nb) relative to the Fernandina lavas of the western Galápagos (Floreana glasses in this  
289 study have mean Ba and Nb contents of  $\sim 310$  ppm and  $\sim 25$  ppm, respectively, relative to Fernandina  
290 glass contents of Ba  $\sim 91$  ppm and Nb  $\sim 23$  ppm – data from Peterson et al., 2017). In addition, the  
291 Floreana glasses have concave-up rare-earth element (REE) patterns, with high light REE/middle REE  
292 ratios (e.g.  $[\text{La}/\text{Sm}]_n$ ) and relatively low middle REE/heavy REE ratios (e.g.  $[\text{Sm}/\text{Yb}]_n$ ) compared to  
293 basalts from the western Galápagos, in agreement with previous geochemical data from Floreana  
294 (Fig. 4). Notably, the deviation between the PEC-corrected trace element (and volatile element) data  
295 is typically smaller than the error associated with SIMS analysis, so the measured values are used in  
296 all discussions below.

#### 297 4.1.2 Volatile elements

298 Substantial heterogeneity is observed in the volatile element concentrations of the Floreana glasses,  
299 with embayments containing lower concentrations of S and H<sub>2</sub>O (~100-1000 ppm and 0.05 – 0.35  
300 wt%, respectively) than the melt inclusions (~1250 ppm S and 0.54 – 0.77 wt% H<sub>2</sub>O; Fig. 5). A positive  
301 correlation is observed between the H<sub>2</sub>O and S concentrations of the Floreana glasses (Fig. 5 & 6).  
302 The CO<sub>2</sub> concentrations measured in the melt inclusions range from ~700 to ~8800 ppm, whereas  
303 the CO<sub>2</sub> concentration of the melt embayments are consistently  $\lesssim$ 2000 ppm (Fig. 5).

304 The F and Cl concentrations of the Floreana melt inclusions and melt embayments range between  
305 458–962 ppm and 360–1144 ppm, respectively. These exceed the concentrations of F and Cl  
306 previously measured in melt inclusions (1–170 ppm Cl) and submarine glasses (376–561 ppm F) from  
307 Fernandina in the western Galápagos (Fig. 7; Koleszar et al., 2009; Peterson et al., 2017). There is no  
308 correlation between the halogen contents of the Floreana glasses and their H<sub>2</sub>O or S contents.  
309 However, correlations are observed between Cl and other highly incompatible trace elements, such  
310 as Ba, Nb and K (Fig. 6).

#### 311 4.1.3 Volatile/non-volatile trace element ratios

312 Volatile to non-volatile trace element ratios that are unfractionated during mantle melting and  
313 crystallisation (owing to their similar bulk partition coefficients) are commonly used to assess the  
314 volatile content of primary mantle melts and their mantle source regions (Cabral et al., 2014; Gibson  
315 and Richards, 2018; Jackson et al., 2015; Métrich et al., 2014; Peterson et al., 2017; Saal et al., 2002;  
316 Shimizu et al., 2016). Additionally, knowledge of the primary volatile to non-volatile trace element  
317 ratios in a system can facilitate calculation of 'original' melt volatile concentrations, prior to  
318 secondary processing (e.g. degassing and diffusive volatile loss; Hartley et al., 2015; Saal et al., 2002).

319 We use the ratios H<sub>2</sub>O/La, F/Nd and Cl/K (and Cl/Nb), which are hypothesised to remain constant  
320 during mantle melting and fractional crystallisation, to investigate variations in the volatile  
321 systematics of the Galápagos basalts (Lassiter et al., 2002; Peterson et al., 2017; Rosenthal et al.,

322 2015; Saal et al., 2002). We primarily consider the H<sub>2</sub>O/La ratio of the Galápagos basalts, instead of  
323 the more commonly used H<sub>2</sub>O/Ce ratio, to interrogate their pre-eruptive H<sub>2</sub>O contents as recent  
324 experimental data indicate that the partitioning behaviour of H<sub>2</sub>O more closely resembles that of La  
325 rather than Ce (see Supplementary Information; Rosenthal et al., 2015). The experimental data for F  
326 partitioning is less clear, with some studies indicating that it has a similar behaviour to La during  
327 mantle melting (Rosenthal et al., 2015), whereas others suggest that it has a similar compatibility to  
328 Pr or Nd (Dalou et al., 2012; Kendrick et al., 2017). Therefore, owing to the uncertainty in the  
329 partitioning of F during mantle melting we consider the ratio F/Nd, as this is the most frequently  
330 used in the literature, to investigate the F contents of the Galápagos basalts and their mantle source  
331 regions. We do, however, acknowledge that variations in the average melt fraction of the Galápagos  
332 mantle could lead to changes in the F/Nd ratio of the erupted basalts if F is less compatible than Nd,  
333 as indicated by the study of Rosenthal et al. (2015). CO<sub>2</sub>/Nb and CO<sub>2</sub>/Ba ratios are not considered in  
334 this study, owing to the strong degassing control on the CO<sub>2</sub> content of the Floreana magmas (see  
335 Section 5); this decouples CO<sub>2</sub> from trace elements with similar bulk partition coefficients during  
336 mantle melting.

337 Considerable variability is observed in the H<sub>2</sub>O/La (45–550), F/Nd (29–47.5) and Cl/K (0.062–0.124)  
338 ratios of the Floreana melt inclusions and embayments (Fig. 7). The Floreana melt inclusion F/Nd  
339 ratios extend to considerably higher values than the F/Nd ratio of basalts from the western  
340 Galápagos (~21; Peterson et al., 2017). In addition, the Cl/K ratio of Floreana glasses are higher than  
341 those of most unaltered/uncontaminated OIBs and MORBs (i.e. 0.01–0.08; Kendrick et al., 2015; Le  
342 Roux et al., 2006; Michael and Cornell, 1998), but are similar to the values measured in basaltic melt  
343 inclusions from HIMU ocean-island basalts (i.e. Mangaia and Rairua; Hanyu et al., 2019). The Cl/Nb  
344 ratio of the Floreana glasses are also higher than most previously measured unaltered MORBs and  
345 OIBs, including the Cl-rich HIMU localities (Floreana Cl/Nb ~ 32.9 ±13.1; Mangaia Cl/Nb <15; Hanyu  
346 et al. 2019).

## 347 4.2 NOMINALLY ANHYDROUS MINERALS

348 We collected H<sub>2</sub>O data from five clinopyroxene and one orthopyroxene crystals from scoria sample  
349 17MMSG16 (28 individual analyses in total), as well as clinopyroxene crystals separated from 3  
350 wehrlite (7 crystals and 17 individual analyses; 17MMSG02b, 17MMSG02c, 17MMSG03a), 2 dunite  
351 (3 crystals and 7 individual analyses; 17MMSG04c, 17MMSG04f), and 2 gabbro xenoliths (6 crystals  
352 and 17 individual analyses; 17MMSG03b, 17MMSG04b). SIMS analyses were carried out on the core  
353 and rim of each crystal (from both the scoria and xenolith samples) to characterise the variability in  
354 H<sub>2</sub>O concentrations across an individual grain. In addition, a small number of core-to-rim profiles  
355 were also collected on the scoria clinopyroxene crystals (Fig. 2; Supplementary Information).

356 Equilibrium melt H<sub>2</sub>O concentrations can be calculated from clinopyroxene and orthopyroxene H<sub>2</sub>O  
357 concentrations through the application of Nernstian H<sup>+</sup> partition coefficients ( $D_H^{pyroxene-melt}$ ). As  
358 the main incorporation mechanism of hydrogen into pyroxene is through the heterovalent coupled  
359 substitution  ${}^{IV}\text{Si}^{4+} = {}^{IV}\text{Al}^{3+} + \text{H}^+$ , the main control on  $D_H^{pyroxene-melt}$  in natural magmatic systems is  
360 thought to be the concentration of tetrahedrally coordinated Al<sup>3+</sup> (O'Leary et al., 2010; Turner et al.,  
361 2017). Clinopyroxene major element compositions, taken from Gleeson et al. (2020a) for each  
362 individual SIMS analysis, are used to calculate  $D_H^{clinopyroxene-melt}$  and  $D_H^{orthopyroxene-melt}$  using  
363 the experimentally-calibrated, temperature-independent parameterisations of O'Leary et al. (2010).  
364 Calculated  $D_H^{pyroxene-melt}$  values are in the range 0.010–0.027, and we obtain similar results using  
365 other parameterisations (Novella et al., 2014; Turner et al., 2017).

### 366 4.2.1 Scoria crystals

367 Clinopyroxene crystals from scoria sample 17MMSG16 have H<sub>2</sub>O contents between 20 and 350 ppm.  
368 In crystals where multiple core analyses were performed, relatively homogeneous core H<sub>2</sub>O  
369 concentrations were observed (<10% variability) with lower H<sub>2</sub>O contents, by ~10-40%, at their rims  
370 (Fig. 2). While this suggests that low pressure degassing has caused diffusive loss of H<sub>2</sub>O from crystal  
371 rims, the relatively homogeneous nature of the crystal cores indicates that diffusive loss of H<sub>2</sub>O



372 during low pressure degassing has a very small influence on these core H<sub>2</sub>O concentrations.  
373 Equilibrium melt H<sub>2</sub>O concentrations calculated from the analyses of the pyroxene cores are typically  
374 between 0.30 and 0.80 wt% but extend up to ~1.6 wt% (partition coefficients calculated using the T-  
375 independent parameterisation of O'Leary et al. 2010).

#### 376 4.2.2 Xenoliths

377 Clinopyroxene crystals in the wehrlitic and dunitic xenoliths have H<sub>2</sub>O concentrations between ~60  
378 and 310 ppm, similar to the range of H<sub>2</sub>O contents observed in clinopyroxene crystals from the  
379 scoria. Multiple analyses of each crystal indicate that the H<sub>2</sub>O concentration of a single crystal is  
380 typically constant (including both core and rim analyses). There is, however, one notable exception;  
381 in crystal 2 from sample 17MMSG03a the measured H<sub>2</sub>O concentrations vary from ~62 ppm to ~259  
382 ppm (lowest H<sub>2</sub>O concentrations are observed near the crystal rim), potentially indicating that this  
383 crystal was influenced by incomplete diffusive re-equilibration with a relatively H<sub>2</sub>O-poor carrier  
384 melt. Using the T-independent parameterisation for H<sub>2</sub>O partitioning into clinopyroxene from  
385 O'Leary et al. (2010), equilibrium-melt H<sub>2</sub>O contents can be determined for each of the  
386 clinopyroxene crystals. In the wehrlitic and dunitic xenoliths, the clinopyroxene analyses indicate a  
387 range of equilibrium melt H<sub>2</sub>O concentrations between ~0.35 and ~1.8 wt%.

388 The H<sub>2</sub>O concentrations measured within clinopyroxene crystals from each of the two gabbroic  
389 xenoliths analysed are relatively constant for each sample (209 ±47 ppm (n=7) and 151 ±29 ppm  
390 (n=10) - 2σ variation). Calculation of equilibrium melt H<sub>2</sub>O concentrations indicates that these  
391 xenoliths last equilibrated with melts containing 1.19 ±0.13 and 0.64 ±0.12 wt% H<sub>2</sub>O, respectively.

## 392 5 DISCUSSION

---

### 393 5.1 VOLATILE SYSTEMATICS IN THE SOUTH-EASTERN GALÁPAGOS ARCHIPELAGO

#### 394 5.1.1 Floreana melt inclusion entrapment pressures

395 The solubility of CO<sub>2</sub> in basaltic magmas is highly sensitive to the pressure of magma storage (Dixon,  
396 1997; Ghiorso and Gualda, 2015; Shishkina et al., 2014). However, using melt inclusion CO<sub>2</sub> contents  
397 to estimate magma storage pressures is complicated by post-entrapment processes, such as  
398 decrepitation (Maclennan, 2017) or migration of CO<sub>2</sub> into a vapour bubble (Steele-Macinnis et al.,  
399 2011; Wieser et al., 2020). Nevertheless, while these post-entrapment processes act to decrease the  
400 CO<sub>2</sub> content of the melt inclusion glass, analysis of the melt phase still permits estimation of  
401 minimum entrapment pressures, which can be compared to other barometric estimates.

402 The apparent entrapment pressures of the Floreana melt inclusions were calculated in the Python  
403 library VESlcal (Iacovino et al., 2020; Wieser et al., 2021) using the H<sub>2</sub>O-CO<sub>2</sub> solubility models of  
404 Ghiorso and Gualda (2015), Iacono-Marziano et al. (2012) and Shishkina et al. (2014). These models  
405 are all calibrated on datasets that overlap with the major element composition of the melt inclusions  
406 in this study and return calculated entrapment pressures that are in close agreement (typically <10  
407 % difference; see Supplementary Information). In detail, our Floreana melt inclusions return  
408 minimum entrapment pressures ranging from ~100 MPa to ~720 MPa, with >50% of inclusions giving  
409 minimum entrapment pressures >450 MPa, consistent with the mineral-melt thermobarometry of  
410 Gleeson et al. (2020a; 717 ±165 MPa). Although ~70% of the inclusions in our samples contain visible  
411 vapour bubbles, our highest calculated entrapment pressure (~720 MPa) is from a bubble free  
412 inclusion. Additionally, we note that high melt inclusion entrapment pressures (>450 MPa) were  
413 obtained from both bubble free and bubble-bearing melt inclusions, indicating that most of the CO<sub>2</sub>  
414 within these bubble-bearing melt inclusions is likely held in the melt phase, consistent with the low  
415 extents of PEC estimated above (Wieser et al., 2020).

416 5.1.2 Degassing and diffusive controls on H<sub>2</sub>O, S and CO<sub>2</sub>

417 Water is more soluble than CO<sub>2</sub> in basaltic melts and OIB magmas are therefore unlikely to degas  
418 substantial amounts of H<sub>2</sub>O until they reach very low pressures, likely within the upper ~1 km of  
419 crust (Dixon, 1997; Ghiorso and Gualda, 2015; Shishkina et al., 2014). Nevertheless, rapid diffusion of  
420 H<sub>2</sub>O (or H<sup>+</sup> ions) in silicate melts and minerals during magma storage, differentiation and ascent can  
421 lead to substantial variability in melt inclusion and embayment H<sub>2</sub>O concentrations and H<sub>2</sub>O/La  
422 ratios.

423 The large range of H<sub>2</sub>O concentrations (0.05–0.77 wt%) and H<sub>2</sub>O/La ratios (~45–550; Fig. 7) in  
424 Floreana melt inclusions and embayments cannot result from magma degassing prior to melt  
425 inclusion or melt embayment formation as melt inclusion CO<sub>2</sub> concentrations and mineral-melt  
426 thermobarometry indicate high pressure storage (Gleeson et al. 2020a). Instead, these data can be  
427 explained through a simple petrogenetic model whereby: (i) melt inclusions with variable H<sub>2</sub>O  
428 contents are trapped in olivine crystals that settle into a cumulate mush; (ii) this mush is  
429 disaggregated shortly prior to eruption and olivine crystals (containing melt inclusions and/or  
430 embayments with diverse geochemical compositions) are entrained into a carrier liquid with a  
431 different H<sub>2</sub>O content to the trapped melts; (iii) owing to the gradient in H<sub>2</sub>O concentrations  
432 between the trapped and external melt, H<sup>+</sup> diffusion drives re-equilibration of the melt inclusion H<sub>2</sub>O  
433 contents with the external melt phase in a matter of hours (Hartley et al., 2015); (iv) syneruptive  
434 degassing of H<sub>2</sub>O from the carrier melt at low pressures drives diffusion of H<sub>2</sub>O out of the melt  
435 embayments and inclusions, potentially reducing the final H<sub>2</sub>O concentration measured in the melt  
436 embayments and some melt inclusions (Fig. 5). The extent of H<sub>2</sub>O loss from the melt embayments  
437 and inclusions during this final step of the model will be controlled by a number of different factors,  
438 including: their initial water contents; the magma ascent rate; the size and shape of the  
439 embayment/inclusions and host crystal; and the temperature of the system (Barth et al., 2019;  
440 Ferguson et al., 2016; Gaetani et al., 2012).

441 The influence of low pressure degassing on the volatile content of the Floreana melt embayments  
442 can be evaluated by modelling magma degassing and diffusive loss of H<sub>2</sub>O, CO<sub>2</sub> and S through an  
443 elongate channel during magma ascent and eruption, i.e. an embayment (Fig. 5; Ferguson et al.,  
444 2016). To do this, we simulate embayment formation and isothermal magma decompression using a  
445 range of starting pressures (250–750 MPa), ascent rates (0.005–0.5 MPa/s), termination pressures  
446 (0.1–0.3 MPa), and initial water contents (0.55–0.95 wt%) at constant initial S (1250 ppm). Diffusive  
447 transport of H<sub>2</sub>O, CO<sub>2</sub>, and S along the modelled embayment was evaluated at 5 μm increments in  
448 embayments of various lengths (100 – 500 μm). At each model step the concentrations of H<sub>2</sub>O, CO<sub>2</sub>  
449 and S in the carrier melt were calculated using the solubility model of Ghiorso and Gualda (2015;  
450 MagmaSat) for H<sub>2</sub>O and CO<sub>2</sub> and Witham et al. (2012; SolEx) for S. These volatile contents were then  
451 used to define the outer boundary condition for the diffusion models. Volatile diffusion within the  
452 melt embayments was then modelled following the method of Ferguson et al. (2016), with H<sub>2</sub>O and  
453 CO<sub>2</sub> diffusivities in basaltic melts from Zhang and Ni (2010), and S diffusivities from Zhang et al.  
454 (2010).

455 The results of our simple diffusion models provide important insights into the volatile content of  
456 magmas beneath Floreana. For example, they indicate that the H<sub>2</sub>O vs S trend in the Floreana  
457 embayments can be reproduced when the initial H<sub>2</sub>O content of the system is between 0.55 and  
458 0.75 wt%, corresponding to the range in H<sub>2</sub>O contents measured in our melt inclusions (Fig. 5). In  
459 addition, the diffusion models also recreate the H<sub>2</sub>O vs CO<sub>2</sub> systematics of the Floreana melt  
460 embayments (Fig. 5).

461 We do not use our diffusion models to estimate the decompression rate of the Floreana magmas, as  
462 we were not able to collect transects along individual embayments (owing to their narrow width and  
463 the relatively large spot size of our analyses; Lloyd et al., 2014), and so our measurements typically  
464 represent a single analysis from each embayment. In addition, the embayments analysed in this  
465 study display a range of morphologies, which will influence the diffusion of volatile species out of the

466 embayments and complicate any estimates of decompression rates based on the simple one-  
467 dimensional diffusion modelling (deGraffenried and Shea, 2021). Nevertheless, as indicated above,  
468 these coupled decompression-diffusion models for a simple melt embayment demonstrate that the  
469 volatile contents of the Floreana embayments are closely reproduced when the initial H<sub>2</sub>O contents  
470 are within the range measured in our Floreana melt inclusions (~0.55–0.75 wt%). This observation is  
471 critical as it indicates that the Floreana melt inclusions re-equilibrated their H<sub>2</sub>O contents with the  
472 carrier melt prior to eruption and thus record the pre-eruptive carrier melt H<sub>2</sub>O content. This  
473 hypothesis is consistent with the geologically fast diffusion of H<sup>+</sup> through the olivine lattice driving  
474 rapid pre-eruptive re-equilibration of melt inclusion H<sub>2</sub>O contents with the external carrier melt (see  
475 step (iii) of the petrogenetic model above; Gaetani et al., 2012; Hartley et al., 2015).

476 Therefore, taking our measured matrix glass La contents and the H<sub>2</sub>O content of our melt inclusions  
477 (i.e. assuming that melt inclusions have diffusively re-equilibrated with the carrier liquid prior to  
478 eruption), we can estimate the H<sub>2</sub>O/La ratio of the pre-eruptive Floreana magma. By doing so, we  
479 can constrain the pre-eruptive melt H<sub>2</sub>O/La ratio to ~270–370, consistent with the H<sub>2</sub>O/La content  
480 measured in a submarine glass sample collected on the flanks of Floreana and analysed by Peterson  
481 et al. (2017; sample DRIFT04 D69b, H<sub>2</sub>O/La ~350). Importantly, this submarine glass has a radiogenic  
482 Pb isotope composition that is similar to the Floreana subaerial basalts and, therefore, is likely  
483 derived from the same magmatic system (Peterson et al., 2017).

484 The Cl/K and Cl/Nb ratios of Floreana submarine glass sample DRIFT04 D69b (0.100 and 28.6,  
485 respectively; Peterson et al., 2017) also closely match those measured in our melt inclusions and  
486 embayments (0.096 ±0.030 and 32.9 ±13.1). Additionally, the correlation between Cl and  
487 incompatible trace elements such as Ba, Nb, and K in the Floreana melt inclusions and embayments  
488 indicates that the Cl concentrations of these glasses, and by extension their H<sub>2</sub>O concentrations, are  
489 not influenced by assimilation of a Cl-rich component (e.g. a hydrothermal brine; Kendrick et al.,  
490 2015). As such, the similarity between the H<sub>2</sub>O/La ratio of Floreana submarine glass DRIFT04 D69b

491 and that estimated from our melt inclusion and embayment analyses supports the interpretation  
492 that our measured melt inclusion H<sub>2</sub>O concentrations are representative of the pre-eruptive carrier  
493 melt H<sub>2</sub>O concentration.

### 494 5.1.3 Heterogeneity in sub-volcanic H<sub>2</sub>O concentrations

495 Previous work on the isotopic composition of cumulate xenoliths from Floreana indicate that  
496 gabbroic xenoliths found in the scoria and lava deposits are isotopically similar to present-day lavas  
497 erupted at Sierra Negra and Cerro Azul volcanoes in the western Galápagos, proximal to the  
498 Galápagos plume stem (Fig. 1; Lyons et al., 2007). Consequently, gabbroic xenoliths, and scoria  
499 crystals that are chemically similar to the gabbroic clinopyroxenes (17MMSG16 crystal 4; Gleeson et  
500 al., 2020a), are interpreted to represent ancient remnants of an earlier period of volcanic activity on  
501 Floreana (>1.5 Ma), before Nazca plate motion carried the island away from the centre of Galápagos  
502 plume upwelling (Lyons et al., 2007). In contrast, wehrlite and dunite xenoliths have isotopic  
503 signatures analogous to recent Floreana lavas and are interpreted to be fragments of the present-  
504 day magmatic system (<1–1.5 Ma; Lyons et al. 2007). As a result, the volatile data collected from  
505 clinopyroxene crystals in the Floreana scoria and cognate xenoliths provide a unique insight into the  
506 H<sub>2</sub>O concentrations of basaltic magmas in the south-eastern Galápagos and, through the >1.5 Ma  
507 gabbroic xenoliths, the western Galápagos Archipelago. Furthermore, because clinopyroxene  
508 crystals from the scoria samples are often derived from liquid-rich magma storage regions and  
509 wehrlite and dunite xenoliths are derived from crystal-rich mush zones (Gleeson et al., 2020a), the  
510 analysis of NAMs in these different sample types can be used to reconstruct the volatile content of  
511 basaltic magmas in different parts of the present day magmatic system (Fig. 8).

512 The yellow field on the right-hand axis of Figure 8 shows a kernel density distribution of melt H<sub>2</sub>O  
513 contents in equilibrium with NAM analyses that are uninfluenced by diffusive loss of H<sub>2</sub>O during low  
514 pressure degassing (i.e., excluding rim analyses that return H<sub>2</sub>O contents >>10% lower than the  
515 respective crystal core) and are derived from the present-day Floreana magmatic system (i.e. those

516 that show no chemical affinity to the gabbroic xenoliths). The kernel density distribution has a  
517 primary peak at ~0.4–0.8 wt% H<sub>2</sub>O, with a long tail to high equilibrium-melt H<sub>2</sub>O contents and a  
518 secondary peak at ~1.5 wt% H<sub>2</sub>O. In addition, a kernel density distribution was also constructed for  
519 the melt H<sub>2</sub>O concentrations predicted from the Floreana whole-rock data, using the measured La  
520 concentrations (Harpp et al., 2014) and an assumed melt H<sub>2</sub>O/La ratio of 350 (grey field in Fig. 8).  
521 While we acknowledge that there might be small differences in the true H<sub>2</sub>O/La of the Floreana  
522 basalts, the kernel density distribution of melt H<sub>2</sub>O concentrations predicted from these whole-rock  
523 analyses display several similarities with that constructed for the NAMs from the present-day  
524 magmatic system, with a primary peak at ~0.4–0.8 wt% H<sub>2</sub>O and a tail to higher H<sub>2</sub>O contents (1–2  
525 wt%; Fig. 8).

526 The overlap between the primary peaks in the two kernel density distributions validates our  
527 calculated equilibrium melt H<sub>2</sub>O concentrations from the NAMs and likely records the typical range  
528 of pre-eruptive melt H<sub>2</sub>O concentrations in the present-day Floreana magmatic system (0.4–0.8 wt%  
529 H<sub>2</sub>O). This is further supported by the similarity between the location of the kernel density  
530 distribution primary peaks and the H<sub>2</sub>O concentrations measured in our Floreana melt inclusions  
531 (0.54–0.77 wt%). However, the subsidiary peak in the NAM equilibrium-melt kernel density  
532 distribution and melt H<sub>2</sub>O concentrations predicted from the whole-rock data record substantially  
533 higher melt H<sub>2</sub>O contents than our Floreana melt inclusions or embayments (Fig. 8).

534 There are two potential origins for the anomalously H<sub>2</sub>O-rich (and trace element enriched) melts  
535 identified from the Floreana NAMs and whole-rock data: (i) they formed from low-fraction mantle  
536 melts generated at the base of the melting region and have incompletely mixed with H<sub>2</sub>O-poor melts  
537 produced at shallower depths; or (ii) they derive from magmas that have undergone chemical  
538 enrichment via reactive porous flow (that is, disequilibrium melt-mush reaction during melt  
539 transport) or *in-situ* crystallisation in highly-crystalline storage regions beneath Floreana (i.e. where  
540 H<sub>2</sub>O and La act as incompatible trace components).

541 To distinguish between these two different possibilities, we can consider the trace element and  
542 isotopic composition of the Floreana basalts (including the enriched samples with estimated H<sub>2</sub>O  
543 concentrations >0.8 wt%). Notably, there is greater heterogeneity in the trace element and isotopic  
544 composition of the Floreana basalts than at any other location in the Galápagos Archipelago,  
545 indicating the presence of a heterogeneous mantle source beneath the island (Harpp et al., 2014).  
546 Importantly, any differences in the lithological properties and/or volatile content of the mantle  
547 components involved in the genesis of the Floreana lavas will cause offsets in their solidus  
548 temperatures and melt productivities. Therefore, variations in the mean melt fraction of the  
549 Floreana mantle source is expected to drive changes in the isotopic composition of the resulting  
550 basalts (by influencing the relative contribution of melts from the different, isotopically distinct,  
551 mantle components) as well as incompatible trace element ratios such as  $[La/Sm]_n$  (where  $n$   
552 indicates normalisation to the primitive mantle composition of Sun and McDonough, 1989). In fact,  
553 when we consider the available isotope and trace element data from the Floreana basalts with  
554 estimated H<sub>2</sub>O concentrations <0.8 wt%, we find that a statistically significant correlation exists  
555 between  $[La/Sm]_n$  and  $^{206}Pb/^{204}Pb$  (Fig. 9). This correlation, however, does not extend to the highly  
556 enriched Floreana basalts (i.e., those that have estimated H<sub>2</sub>O contents >0.8 wt%), which are  
557 isotopically indistinguishable from the rest of the Floreana lavas. We therefore suggest that their  
558 anomalous trace element signature is a consequence of crustal processing in magmatic mush zones,  
559 rather than variations in the extent of mantle melting (Fig. 9; Gleeson et al., 2020a; Harpp et al.,  
560 2014; Lyons et al., 2007).

561 In addition, there is substantial geochemical and textural evidence preserved in the Floreana  
562 xenoliths to support the interpretation that reactive porous flow is an important geochemical  
563 process in mush zones beneath the island. For example, trace element enrichment in the wehrlite  
564 xenoliths cannot be explained through simple fractional crystallisation, but can be explained by  
565 models that account for melt-mush reaction during reactive porous flow (Gleeson et al., 2020a).  
566 Additionally, the enrichment in the trace element composition of the cumulate clinopyroxenes are



567 commonly more extreme at the crystal rims compared to their cores, consistent with trace element  
568 enrichment originating through magma processing in a mush rather than initial crystallisation from  
569 anomalously enriched mantle melts (Gleeson et al. 2020a). Finally, all clinopyroxene crystals that  
570 have anomalously high equilibrium-melt H<sub>2</sub>O contents also have incompatible trace element  
571 signatures that are too enriched to be in equilibrium with the majority of the erupted Floreana  
572 basalts (Gleeson et al., 2020a), and, as a result, we favour the reactive porous flow hypothesis  
573 presented above.

574 In summary, the kernel density distributions calculated for the melt H<sub>2</sub>O contents in equilibrium with  
575 the Floreana NAMs and the predicted melt H<sub>2</sub>O concentrations calculated via whole-rock trace  
576 element data (i.e. La concentrations) have primary peaks at ~0.4–0.8 wt% H<sub>2</sub>O. This represents the  
577 typical H<sub>2</sub>O concentration of Floreana sub-volcanic melts which have not been modified by cumulate  
578 processes. However, reactive porous flow in highly crystalline magma storage regions generates  
579 local incompatible trace element-enrichment (Gleeson et al. 2020a), resulting in melts with H<sub>2</sub>O  
580 concentrations >>0.8 wt%. Rare, trace element enriched, whole-rock samples from Floreana (with  
581 estimated H<sub>2</sub>O concentrations >0.8 wt%) likely contain a substantial contribution of melts which  
582 have undergone geochemical enrichment by reactive porous flow, and indicate that melts in highly  
583 crystalline sub-volcanic storage regions are occasionally remobilised and erupted.

## 584 5.2 VOLATILE SYSTEMATICS IN THE WESTERN GALÁPAGOS ARCHIPELAGO

585 While our new data represents the first systematic constraints on the volatile contents of the  
586 Floreana magmas in the south-eastern Galápagos, published volatile data provides insights into the  
587 volatile systematics of the western Galápagos volcanic systems. For example, Peterson et al. (2017)  
588 report the volatile content (H<sub>2</sub>O, F, Cl, S, and CO<sub>2</sub>) of submarine glasses collected from a series of  
589 dredging expeditions across the Galápagos Platform. Included within their dataset is a suite of  
590 submarine basalts from the western margin of Fernandina, at the leading edge of the Galápagos  
591 mantle plume (Fig. 1). These basalts have high <sup>3</sup>He/<sup>4</sup>He ratios that are characteristic of Fernandina

592 magmas (Harpp and White, 2001; Peterson et al. 2017). In addition, olivine-hosted melt inclusions  
593 from a nearby submarine lava flow on the western margin of Fernandina have also been analysed  
594 for their volatile contents (Fig. 1). Together, these submarine glass and melt inclusion analyses  
595 provide important insights into the volatile systematics of the Fernandina magmatic system and, by  
596 comparing our new Floreana data with these published volatile records, allow us to investigate the  
597 magmatic volatile contents in two regions of the archipelago with highly contrasting magmatic  
598 storage conditions and eruptive styles (Gleeson et al., 2020a; Harpp and Geist, 2018; Stock et al.,  
599 2020).

600 The Fernandina melt inclusions show a positive correlation between Cl and incompatible trace  
601 element concentrations (e.g. Nb, K; Fig. 10; Koleszar et al., 2009), with Cl/K ratios of  $0.038 \pm 0.016$ ,  
602 consistent with the similar compatibilities of these elements during mantle melting (Lassiter et al.,  
603 2002). In contrast, matrix glasses in the Fernandina submarine lavas have a narrow range of K and  
604 Nb concentrations, but a relatively large range of Cl concentrations (~150–450 ppm Cl) and thus  
605 variable Cl/K ratios (Fig. 10; Peterson et al., 2017). This variability in the Cl/K ratio of the Fernandina  
606 submarine glasses likely reflects assimilation of a Cl-rich component, such as a hydrothermal brine  
607 (Jackson et al., 2015; Kendrick et al., 2015). Additionally, the correlation between Cl concentrations  
608 and H<sub>2</sub>O/La ratios in the Fernandina submarine matrix glasses ( $r^2=0.723$ ), indicates that brine  
609 assimilation has also impacted on their H<sub>2</sub>O concentrations (Fig. 10).

610 By considering volatile and non-volatile trace element systematics in the Fernandina matrix glasses,  
611 it is possible to calculate the extent of Cl and H<sub>2</sub>O assimilation (Kendrick et al., 2015). First, the  
612 amount of Cl that was assimilated by each sample can be estimated by calculating the amount of Cl  
613 required to match the Cl/K ratio of the Fernandina melt inclusions (0.038) and subtracting this from  
614 the measured Cl concentration. The amount of assimilated H<sub>2</sub>O can then be calculated if the H<sub>2</sub>O/Cl  
615 ratio of the assimilated component can be determined, which is achieved by taking the intercept of a  
616 linear regression through the glass data on plots of H<sub>2</sub>O/Cl vs K/Cl or F/Cl (Kendrick et al., 2015). The

617 Fernandina submarine matrix glasses of Peterson et al. (2017) show a linear correlation between  
618  $H_2O/Cl$  and  $K/Cl$ , which indicates that the assimilated brine component has a  $H_2O/Cl$  ratio of  $\sim 17.1$   
619 (Fig. 10). Therefore, using the calculated amount of  $Cl$  assimilated by each sample, and the  $H_2O/Cl$   
620 ratio of the assimilated component, it is possible to calculate the amount of  $H_2O$  that has been  
621 assimilated.

622 The kernel density distribution of the uncorrected Fernandina matrix glass  $H_2O/La$  ratio is centred at  
623  $\sim 500$ , with a long tail extending to higher values ( $>800$ ; Fig. 10). However, using the method above,  
624 we can correct the  $H_2O$  content of the Fernandina submarine glasses to account for the influence of  
625 brine assimilation. After correction, the data forms a Gaussian distribution with a mean  $H_2O/La$  ratio  
626 of 410, spread over a narrow range of values ( $2\sigma = 83$ ; Fig. 10). These corrected data give the  $H_2O/La$   
627 ratios of the Fernandina primary melts, with the narrow range reflecting their limited  $H_2O/La$   
628 variability, consistent with the elemental and isotopic homogeneity of Fernandina erupted basalts  
629 (Geist et al., 2014; Harpp and Geist, 2018).

630 The  $H_2O$  content of olivine-hosted melt inclusions from Fernandina are also influenced by secondary  
631 processes (Koleszar et al., 2009), as indicated by their constant  $H_2O$  contents (0.8 – 1.0 wt%) and  
632  $H_2O/La$  ratios that extend to high values ( $>800$ ; Fig. 10). The high  $H_2O/La$  ratios of some of the  
633 Fernandina melt inclusions can be explained by diffusive hydration of primitive melt inclusions (with  
634 low initial concentrations of  $H_2O$ ) as their host olivine crystals are entrained into a more evolved  
635 (and thus  $H_2O$ -rich) magma prior to eruption. As  $H^+$  diffuses significantly faster than  $La$  through the  
636 olivine crystal lattice, the  $H_2O$  concentration of the olivine-hosted melt inclusions will re-equilibrate  
637 with the external  $H_2O$ -rich melt ( $\sim 0.8 - 1$  wt%  $H_2O$ ) on timescales of hours-to-days (Fig. 10; Gaetani et  
638 al., 2012). In contrast, the melt inclusion  $La$  concentrations will remain constant over long timescales  
639 (as diffusion of  $La$  is several orders of magnitude slower than that of  $H_2O$  through silicate melts and  
640 olivine host crystals; Zhang et al., 2010; Zhang and Ni, 2010), resulting in high  $H_2O/La$  ratios (Hartley  
641 et al., 2015).

642 Using the H<sub>2</sub>O/La ratio of the Fernandina submarine glasses, corrected for brine assimilation, we can  
643 estimate the H<sub>2</sub>O contents of the Fernandina melt inclusions at the time of entrapment (by taking  
644 the PEC corrected La concentrations of Koleszar et al., 2009). The predicted H<sub>2</sub>O concentrations vary  
645 from ~0.1 to 0.62 wt%, with the most primitive melt inclusions showing the greatest variability in  
646 H<sub>2</sub>O contents. More evolved (lower Mg#) melt inclusions typically have a more restricted range of  
647 H<sub>2</sub>O concentrations and the mean H<sub>2</sub>O concentrations increase with decreasing Mg# and olivine Fo  
648 content, consistent with H<sub>2</sub>O behaving as an incompatible element during concurrent mixing and  
649 crystallisation (Fig. 8). The brine-corrected H<sub>2</sub>O contents of the Fernandina submarine glasses plot  
650 along the same fractional crystallisation trajectory as the mean composition of the melt inclusions.  
651 As a result, the Fernandina melt inclusion and submarine glass data indicate that the Fernandina  
652 magmas are controlled by concurrent mixing and crystallisation of mantle-derived melts (Koleszar et  
653 al., 2009; Maclennan, 2008).

654 Furthermore, as gabbroic xenoliths from Floreana are hypothesised to sample an ancient magmatic  
655 system, i.e. from when the island was located close to the Galápagos plume stem (Lyons et al.,  
656 2007), we would expect our new clinopyroxene volatile data from these nodules to match the  
657 volatile contents of erupted products from present-day plume-proximal volcanoes in the western  
658 archipelago. In fact, the calculated equilibrium melt H<sub>2</sub>O contents from one of our gabbroic xenoliths  
659 (17MMSG04b; 0.64 ± 0.12 wt%) does overlap with the brine-corrected H<sub>2</sub>O concentrations in the  
660 submarine glasses from the western archipelago (Peterson et al., 2017), but those in our other  
661 gabbroic sample (17MMSG03b; 1.19 ± 0.13 wt%) are significantly higher than typical melt H<sub>2</sub>O  
662 analyses from the western Galápagos Archipelago. The clinopyroxene H<sub>2</sub>O contents of these two  
663 gabbroic xenoliths are unlikely to be related to each other by simple fractional crystallisation as the  
664 clinopyroxene crystals from both xenoliths have similar major element signatures (e.g., Mg#;  
665 Gleeson et al. 2020a). Instead, the high H<sub>2</sub>O concentrations observed in clinopyroxene crystals from  
666 sample 17MMSG03b might record geochemical enrichment by the same reactive porous flow  
667 process that has been identified in cumulate mush zones beneath Floreana (Gleeson et al., 2020a),

668 but more data is required to confirm this hypothesis. As a result, the high H<sub>2</sub>O concentrations  
669 measured in gabbro 17MMSG03b could indicate that reactive porous flow operates beneath  
670 present-day volcanoes in the western archipelago, but is yet to be identified in erupted products  
671 (signatures of reactive porous flow in erupted magmas may include an over-enrichment in  
672 incompatible trace elements with increasing differentiation; Lissenberg and MacLeod, 2016); the  
673 ancient Floreana magmatic system was distinct from the magmatic systems currently underlying the  
674 plume-proximal western volcanoes (Harpp and Geist, 2018); or that the H<sub>2</sub>O content of the gabbroic  
675 xenoliths is reset by interaction with more recent Floreana magmas.

### 676 5.3 CONTRASTING FERNANDINA AND FLOREANA BASALT H<sub>2</sub>O CONCENTRATIONS

677 Our new data from the Floreana basalts and xenoliths, and re-evaluation of published data from  
678 Fernandina, indicate that these volcanoes have distinct volatile histories: the H<sub>2</sub>O contents of the  
679 Fernandina basalts are primarily controlled by fractional crystallisation and magma mixing, whereas  
680 some Floreana basalts are influenced by H<sub>2</sub>O-rich magmas generated by reactive porous flow within  
681 crystal-rich sub-volcanic mush zones. To directly compare the volatile contents of magmas from  
682 these locations, we reconstruct initial melt inclusion and whole-rock H<sub>2</sub>O concentrations (i.e. prior to  
683 alteration by secondary processes) using their measured La concentrations and the characteristic  
684 H<sub>2</sub>O/La ratio of each magmatic system as determined above.

685 Comparing reconstructed initial melt inclusion and whole-rock H<sub>2</sub>O concentrations indicates that the  
686 Floreana magmas typically have slightly higher H<sub>2</sub>O contents than the Fernandina magmas at an  
687 equivalent melt Mg# (Fig. 8). For example, at Mg# ~0.65, Floreana magmas contain ~0.4–0.8 wt%  
688 H<sub>2</sub>O (0.6 wt% average), whereas Fernandina magmas contain 0.1–0.67 wt% H<sub>2</sub>O (0.4 wt% average;  
689 Fig. 8; Koleszar et al., 2009; Peterson et al., 2017). Harpp et al. (2014) hypothesised that the  
690 abundance of explosive volcanism on Floreana might be due to high magmatic H<sub>2</sub>O contents.  
691 However, we suggest that the difference in magmatic H<sub>2</sub>O concentrations at Floreana and  
692 Fernandina is too small to account for their different eruptive styles, especially as Fernandina

693 magmas typically erupt at lower MgO concentrations when they have very similar H<sub>2</sub>O contents to  
694 the more mafic erupted melts on Floreana.

## 695 **6 INSIGHTS INTO THE VOLATILE CONTENT OF THE GALÁPAGOS MANTLE** 696 **SOURCE**

---

### 697 **6.1 THE H<sub>2</sub>O SYSTEMATICS OF THE GALÁPAGOS MANTLE PLUME**

698 Radiogenic isotope, trace element, and major element data indicate that the Galápagos mantle  
699 plume is heterogeneous over a variety of length-scales (Gibson et al., 2012; Gleeson et al., 2021;  
700 Harpp and White, 2001). In fact, the mantle sources of the Floreana and Fernandina basalts likely  
701 contain at least 2 distinct components that may have different volatile contents or lithological  
702 properties and may thus be characterised by different solidus temperatures and melt productivities  
703 (Harpp et al., 2014; Katz et al., 2003; Lambart et al., 2016). Therefore, to determine the contribution  
704 of each source component to the trace element budget of the Fernandina and Floreana basalts, and  
705 by extension constrain the source volatile contents, we require knowledge of the source trace  
706 element compositions, source proportions and melting behaviours (e.g. Rudge et al., 2013).  
707 However, accurate constraints on the trace element composition of the mantle source components,  
708 and their relative proportions in the Galápagos mantle plume, are not currently available.

709 For example, the Fernandina basalts have unradiogenic He isotope ratios ( $^3\text{He}/^4\text{He} \sim 30 R/R_A$ ), which  
710 has been used to suggest that a primordial or primitive mantle component is present in the mantle  
711 source region of the Fernandina basalts (Kurz et al., 2009). In fact, previous studies have estimated  
712 the H<sub>2</sub>O content of the Fernandina mantle source through the combination of measured H<sub>2</sub>O/Ce  
713 ratios and published estimates for the trace element composition of the primitive mantle (Peterson  
714 et al., 2017). Yet, both the trace element systematics (e.g. the high TITAN signature; that is, high  
715 primitive mantle normalised concentrations of Ti, Ta, and Nb relative to elements with similar  
716 compatibilities during mantle melting) and radiogenic isotope composition of the Fernandina basalts

717 do not match those expected from melting of a primitive mantle component (Farley et al., 1992;  
718 Harpp and Weis, 2020; Harpp and White, 2001; Jackson et al., 2008). As a result, there is substantial  
719 evidence to suggest that a primitive mantle trace element composition is not appropriate for the  
720 Fernandina source and could lead to significant errors in the estimated source H<sub>2</sub>O concentrations if  
721 used in this manner. Moreover, He might be decoupled from lithophile elements such as Sr or La  
722 during mantle melting (Graham et al., 2014), further demonstrating that high <sup>3</sup>He/<sup>4</sup>He ratios alone  
723 cannot be used to justify the use of a primitive mantle trace element estimate for the Fernandina  
724 mantle source.

725 No robust estimates exist for the trace element composition of the Floreana mantle source. Recent  
726 work has shown that the radiogenic Pb isotope composition of the Floreana basalts in the south-  
727 eastern Galápagos is similar to that of the global HIMU mantle (Chauvel et al., 1992; Harpp et al.,  
728 2014; Weiss et al., 2016) and an estimate for the trace element composition of the HIMU mantle  
729 was proposed by Weiss et al. (2016). However, there are several key differences between the  
730 Floreana basalts and typical HIMU basalts that indicate that the Weiss et al. (2016) estimate for the  
731 trace element composition of the HIMU mantle is unlikely to be appropriate for the Floreana mantle  
732 source. For example, the Floreana basalts contain more radiogenic <sup>87</sup>Sr/<sup>86</sup>Sr signatures than typical  
733 HIMU basalts (Harpp and White, 2001) and the high Pb concentration of most Floreana lavas, and  
734 therefore their low Ce/Pb ratios, are inconsistent with the signatures expected for true HIMU basalts  
735 (Harpp et al., 2014). As a result, using published estimates for the trace element composition of the  
736 primitive mantle and HIMU source to determine the H<sub>2</sub>O content of the Fernandina and Floreana  
737 mantle source regions, respectively, is not appropriate.

738 More work is required to accurately determine the trace element composition of the various mantle  
739 components in the Galápagos plume. One promising method that may provide future insights into  
740 the composition of the Galápagos plume is the integration of multi-component mantle melting  
741 models with Markov Chain Monte Carlo algorithms (e.g. Brown et al., 2020; Gleeson et al., 2020b).

742 Nevertheless, in the absence of accurate source trace element estimates, we can consider the  
743 H<sub>2</sub>O/REE systematics of the Galápagos basalts to determine the relative ‘hydration’ of the different  
744 Galápagos source components with respect to their trace element composition. Specifically, we can  
745 use our new data, alongside published volatile analyses from basalts across the archipelago and  
746 nearby spreading centre (Cushman et al., 2004; Gleeson and Gibson, 2021; Ingle et al., 2010;  
747 Koleszar et al., 2009; Peterson et al., 2017), to investigate how the H<sub>2</sub>O/REE systematics of the  
748 Galápagos basalts are related to the extent of geochemical enrichment.

749 The H<sub>2</sub>O/La systematics of the depleted peridotite component in the Galápagos mantle plume (the  
750 Depleted Galápagos Mantle; DGM) has recently been determined through analysis of plume-  
751 influenced MORBs along the Galápagos Spreading Centre (GSC; Gleeson and Gibson, 2021). This data  
752 revealed that isotopically depleted basalts associated with the Galápagos plume (that have not been  
753 influenced by assimilation of Cl-rich brine components) have H<sub>2</sub>O/La ratios of ~750. In contrast, trace  
754 element and isotopically enriched basalts from the GSC (i.e. with [La/Sm]<sub>n</sub>>2) exhibit H<sub>2</sub>O/La ratios of  
755 350 – 400, similar to the H<sub>2</sub>O/La ratios observed in the Fernandina and Floreana basalts (410 ±82 and  
756 270 – 370, respectively; Fig. 11).

757 Overall, these data indicate that the H<sub>2</sub>O/La ratio of the enriched mantle components in the  
758 Galápagos plume are lower than that of the DGM. This ‘dehydration’ signature indicates that the  
759 H<sub>2</sub>O<sup>enr</sup>/H<sub>2</sub>O<sup>DGM</sup> ratio of the Galápagos mantle plume (i.e. the concentration of H<sub>2</sub>O in the enriched  
760 source components relative to the DGM) is smaller than La<sup>enr</sup>/La<sup>DGM</sup>. Notably, the ‘dehydration’  
761 signature is also observed when we consider the H<sub>2</sub>O/Ce ratio of the enriched Galápagos basalts  
762 instead of H<sub>2</sub>O/La. In particular, the H<sub>2</sub>O/Ce ratio of basalts from Fernandina and Floreana are <200  
763 (based on our analysis above), whereas depleted plume-influenced GSC basalts have H<sub>2</sub>O/Ce ratios  
764 between 200 and 250 (Fig. 11; Gleeson and Gibson, 2021).

765 The origin of these differences in the H<sub>2</sub>O/REE systematics of the Galápagos plume basalts is  
766 uncertain, but it is notable that this is not the only region globally where such variations have been



767 observed. In fact, similar or even larger variations are observed in the H<sub>2</sub>O/La and H<sub>2</sub>O/Ce ratio of  
768 MORBs and OIBs worldwide. For example, MORBs erupted north of Iceland along the Mid-Atlantic  
769 Ridge have H<sub>2</sub>O/Ce ratios of 280 ±37 (Michael, 1995), whereas EM-type basalts erupted in the  
770 northern Pacific (between 0°N and 20°N along the East Pacific Rise) have H<sub>2</sub>O/Ce ratios of only 110  
771 ±20 (Dixon et al., 2017). The origin of these variations in the H<sub>2</sub>O/REE systematics of MORBs and  
772 OIBs remains debated, but both dehydration of the slab during subduction and diffusive loss of H<sub>2</sub>O  
773 from enriched components in the mantle may play an important role in the formation of enriched  
774 mantle components with relatively low H<sub>2</sub>O/La and H<sub>2</sub>O/Ce systematics (Cabral et al., 2014; Dixon et  
775 al., 2017).

## 776 6.2 HALOGEN-RICH NATURE OF THE FLOREANA MANTLE SOURCE

777 As our new data from the Floreana melt inclusions and melt embayments reveals correlations  
778 between Cl and highly incompatible trace elements (e.g. Ba, K) and no significant correlation  
779 between the halogens (F and Cl) and H<sub>2</sub>O or S (at the 95% significance level), the measured  
780 concentrations of F and Cl in the Floreana glasses are unlikely to be influenced by secondary  
781 processes such as degassing or brine assimilation (Fig. 6). Therefore, the F/Nd and Cl/K ratios  
782 measured in the Floreana melt inclusions and embayments (35.1 ±5.1 and 0.096 ±0.030,  
783 respectively) can be used to qualitatively evaluate the F and Cl content of the FLO mantle source  
784 (assuming that these ratios are unfractionated during mantle melting). Notably, our measured  
785 Floreana melt F/Nd and Cl/K ratios are substantially higher and more variable than in erupted basalts  
786 from Fernandina in the western Galápagos (F/Nd ~20.2, Cl/K ~0.038; Koleszar et al., 2009; Peterson  
787 et al., 2017; Fig. 7) and plume influenced basalts from the GSC (Gleeson and Gibson, 2021).

788 The high <sup>206</sup>Pb/<sup>204</sup>Pb mantle source beneath Floreana (i.e., the FLO mantle; Harpp and Weis, 2020;  
789 Harpp and White, 2001), therefore, appears to be unique in the Galápagos, not only for its isotopic  
790 composition but also its halogen content. In addition, if we assume that contribution of melts from  
791 other mantle source components to the Floreana basalts will lead to a decrease in the F/Nd and Cl/K

792 ratios of the Floreana basalts, we can take the highest values measured in our melt inclusions and  
793 embayments to place constraints on the minimum F/Nd and Cl/K ratios of the Galápagos FLO mantle  
794 (47.5 and 0.124, respectively).

795 Comparison of our new Floreana data with other global OIBs reveals that such high F/Nd and Cl/K  
796 ratios are very rare (Kendrick et al., 2014; Métrich et al., 2014; Sides et al., 2014; Workman et al.,  
797 2006; Fig. 7). In fact, comparable F/Nd and Cl/K values have only been identified at localities that are  
798 dominated by melting of a HIMU mantle source (e.g. Mangaia and Tubuai; Cabral et al., 2014; Hanyu  
799 et al., 2019). Therefore, our new data suggests that true HIMU localities are not the only regions in  
800 the Earth's mantle that can contain high concentrations of F and Cl, and indicates that the FLO  
801 mantle source might be an important reservoir of halogens in the Galápagos mantle plume (despite  
802 its relatively localised influence).

## 803 7 CONCLUSIONS

---

804 By integrating volcanic glass and NAM analyses from different parts of the Galápagos Archipelago,  
805 we gain new insights into the behaviour and mantle source contents of volatiles across a single OIB  
806 system. The H<sub>2</sub>O contents of submarine glasses (corrected for brine assimilation) and melt inclusions  
807 from Fernandina indicate that magma volatile contents in the western Galápagos Archipelago are  
808 primarily controlled by concurrent mixing and crystallisation of heterogeneous mantle melts. In  
809 contrast, our new data from Floreana reveal that magma volatile contents in the south-eastern  
810 Galápagos Archipelago are affected by reactive porous flow through crystal-rich mush zones. Despite  
811 these different processes controlling volatile behaviour during magmatic evolution, the pre-eruptive  
812 H<sub>2</sub>O contents of Floreana and Fernandina magmas are likely very similar (~0.4–0.9 wt%), suggesting  
813 that differences in the style of volcanic activity on the two islands are not driven by differences in  
814 their volatile contents.

815 Calculating the volatile contents of mantle source components contributing to erupted basalts on  
816 Floreana and Fernandina is inhibited by uncertainties in their trace element compositions and  
817 relative proportions. Nevertheless, our new data indicates that the enriched mantle components in  
818 the Galápagos plume are characterised by lower H<sub>2</sub>O/La ratios than the DGM, and a relative  
819 dehydration of these enriched components with respect to their trace element compositions.  
820 Furthermore, our data reveals that the Floreana basalts have high F/Nd and Cl/K ratios, are 2-3 time  
821 greater than those measured in other parts of the Galápagos Archipelago and may indicate that the  
822 FLO mantle source represents an important reservoir of halogens in the Galápagos plume.

## 823 CODE AVAILABILITY

---

824 Add code developed for this study are available via  
825 <https://github.com/gleesonm1/MagmaDecompress>

## 826 ACKNOWLEDGEMENTS

---

827 This study was supported by a NERC (Natural Environmental Research Council) Research Training  
828 Student Grant (NE/L002507/1) awarded to M.L.M.G, as well as grant from the Darwin Galápagos  
829 Fund awarded to S.A.G. M. J. S. was supported by a Charles Darwin and Galápagos Islands Junior  
830 Research Fellowship at Christ's College, Cambridge. SIMS analysis was made possible by the NERC  
831 IMF grant IMF622/0517. We are grateful to Iris Buisman for help with EPMA analysis and SEM  
832 images. We thank Margaret Hartley for comments on an early version of this manuscript and are  
833 grateful for the support of the Charles Darwin Research Station and the Galápagos National Park  
834 authorities for their assistance with fieldwork. Antonio Proaño, Lenin Cruz and the crew of the Pirata  
835 provided invaluable help in the field.

836

## 837 REFERENCES

---

- 838 Adam, J., Turner, M., Hauri, E.H., Turner, S., 2016. Crystal/melt partitioning of water and other  
839 volatiles during the near-solidus melting of mantle peridotite: Comparisons with non-volatile  
840 incompatible elements and implications for the generation of intraplate magmatism. *Am.*  
841 *Mineral.* 101, 876–888. <https://doi.org/10.2138/am-2016-5437>
- 842 Allan, J.F., Simkin, T., 2000. Fernandina Volcano's evolved, well-mixed basalts: Mineralogical and  
843 petrological constraints on the nature of the Galapagos plume. *J. Geophys. Res. Solid Earth*  
844 105, 6017–6041. <https://doi.org/10.1029/1999JB900417>
- 845 Asimow, P.D., Dixon, J.E., Langmuir, C.H., 2004. A hydrous melting and fractionation model for mid-  
846 ocean ridge basalts: Application to the Mid-Atlantic Ridge near the Azores. *Geochem.*  
847 *Geophys. Geosystems* 5, n/a-n/a. <https://doi.org/10.1029/2003GC000568>

848 Asimow, P.D., Langmuir, C.H., 2003. The importance of water to oceanic mantle melting regimes.  
849 Nature 421, 815–820. <https://doi.org/10.1038/nature01429>

850 Barth, A., Newcombe, M., Plank, T., Gonnermann, H., Hajimirza, S., Soto, G.J., Saballos, A., Hauri, E.,  
851 2019. Magma decompression rate correlates with explosivity at basaltic volcanoes —  
852 Constraints from water diffusion in olivine. *J. Volcanol. Geotherm. Res.* 387, 106664.  
853 <https://doi.org/10.1016/j.jvolgeores.2019.106664>

854 Bow, C.S., Geist, D.J., 1992. Geology and petrology of Floreana Island, Galapagos Archipelago,  
855 Ecuador. *J. Volcanol. Geotherm. Res.* 52, 83–105. [https://doi.org/10.1016/0377-](https://doi.org/10.1016/0377-0273(92)90134-Y)  
856 [0273\(92\)90134-Y](https://doi.org/10.1016/0377-0273(92)90134-Y)

857 Brown, E.L., Petersen, K.D., Leshner, C.E., 2020. Markov chain Monte Carlo inversion of mantle  
858 temperature and source composition, with application to Reykjanes Peninsula, Iceland.  
859 *Earth Planet. Sci. Lett.* 532, 116007. <https://doi.org/10.1016/j.epsl.2019.116007>

860 Cabral, R.A., Jackson, M.G., Koga, K.T., Rose-Koga, E.F., Hauri, E.H., Whitehouse, M.J., Price, A.A.,  
861 Day, J.M.D., Shimizu, N., Kelley, K.A., 2014. Volatile cycling of H<sub>2</sub>O, CO<sub>2</sub>, F, and Cl in the  
862 HIMU mantle: A new window provided by melt inclusions from oceanic hot spot lavas at  
863 Mangaia, Cook Islands. *Geochem. Geophys. Geosystems* 15, 4445–4467.  
864 <https://doi.org/10.1002/2014GC005473>

865 Chadwick, W.W., Jónsson, S., Geist, D.J., Poland, M., Johnson, D.J., Batt, S., Harpp, K.S., Ruiz, A.,  
866 2011. The May 2005 eruption of Fernandina volcano, Galápagos: The first circumferential  
867 dike intrusion observed by GPS and InSAR. *Bull. Volcanol.* 73, 679–697.  
868 <https://doi.org/10.1007/s00445-010-0433-0>

869 Chauvel, C., Hofmann, A.W., Vidal, P., 1992. himu-em: The French Polynesian connection. *Earth*  
870 *Planet. Sci. Lett.* 110, 99–119. [https://doi.org/10.1016/0012-821X\(92\)90042-T](https://doi.org/10.1016/0012-821X(92)90042-T)

871 Costa, F., Shea, T., Ubide, T., 2020. Diffusion chronometry and the timescales of magmatic processes.  
872 *Nat. Rev. Earth Environ.* <https://doi.org/10.1038/s43017-020-0038-x>

873 Cushman, B., Sinton, J., Ito, G., Eaby Dixon, J., 2004. Glass compositions, plume-ridge interaction, and  
874 hydrous melting along the Galápagos Spreading Center, 90.5°W to 98°W. *Geochem.*  
875 *Geophys. Geosystems* 5. <https://doi.org/10.1029/2004GC000709>

876 Dalou, C., Koga, K. T., Shimizu, N., 2012. Experimental determination of F and Cl partitioning  
877 between lherzolite and basaltic melt. *Contrib. Mineral. Petrol.* 163, 591–609.

878 Danyushevsky, L.V., Plechov, P., 2011. Petrolog3: Integrated software for modeling crystallization  
879 processes. *Geochem. Geophys. Geosystems* 12, n/a-n/a.  
880 <https://doi.org/10.1029/2011GC003516>

881 deGraffenried, R.L., Shea, T., 2021. Using Volatile Element Concentration Profiles in Crystal-Hosted  
882 Melt Embayments to Estimate Magma Decompression Rate: Assumptions and Inherited  
883 Errors. *Geochem. Geophys. Geosystems* 22. <https://doi.org/10.1029/2021GC009672>

884 Dixon, J.E., 1997. Degassing of alkalic basalts. *Am. Mineral.* 82, 368–378.  
885 <https://doi.org/10.2138/am-1997-3-415>

886 Dixon, J.E., Bindeman, I.N., Kingsley, R.H., Simons, K.K., Le Roux, P.J., Hajewski, T.R., Swart, P.,  
887 Langmuir, C.H., Ryan, J.G., Walowski, K.J., Wada, I., Wallace, P.J., 2017. Light Stable Isotopic  
888 Compositions of Enriched Mantle Sources: Resolving the Dehydration Paradox. *Geochem.*  
889 *Geophys. Geosystems* 18, 3801–3839. <https://doi.org/10.1002/2016GC006743>

890 Edmonds, M., Kohn, S.C., Hauri, E.H., Humphreys, M.C.S., Cassidy, M., 2016. Extensive, water-rich  
891 magma reservoir beneath southern Montserrat. *Lithos* 252–253, 216–233.  
892 <https://doi.org/10.1016/j.lithos.2016.02.026>

893 Farley, K.A., Natland, J.H., Craig, H., 1992. Binary mixing of enriched and undegassed (primitive?)  
894 mantle components (He, Sr, Nd, Pb) in Samoan lavas. *Earth Planet. Sci. Lett.* 111, 183–199.  
895 [https://doi.org/10.1016/0012-821X\(92\)90178-X](https://doi.org/10.1016/0012-821X(92)90178-X)

896 Ferguson, D.J., Gonnermann, H.M., Ruprecht, P., Plank, T., Hauri, E.H., Houghton, B.F., Swanson,  
897 D.A., 2016. Magma decompression rates during explosive eruptions of Kīlauea volcano,

898 Hawaii, recorded by melt embayments. *Bull. Volcanol.* 78, 71.  
899 <https://doi.org/10.1007/s00445-016-1064-x>

900 Ferriss, E., Plank, T., Walker, D., 2016. Site-specific hydrogen diffusion rates during clinopyroxene  
901 dehydration. *Contrib. Mineral. Petrol.* 171, 55. <https://doi.org/10.1007/s00410-016-1262-8>

902 Friedman, I., Long, W., 1976. Hydration Rate of Obsidian. *Science* 191, 347–352.  
903 <https://doi.org/10.1126/science.191.4225.347>

904 Gaetani, G.A., Grove, T.L., 1998. The influence of water on melting of mantle peridotite. *Contrib.*  
905 *Mineral. Petrol.* 131, 323–346. <https://doi.org/10.1007/s004100050396>

906 Gaetani, G.A., O’Leary, J.A., Shimizu, N., Bucholz, C.E., Newville, M., 2012. Rapid reequilibration of  
907 H<sub>2</sub>O and oxygen fugacity in olivine-hosted melt inclusions. *Geology* 40, 915–918.  
908 <https://doi.org/10.1130/G32992.1>

909 Geist, D.J., Bergantz, G., Chadwick, W.W., 2014. Galápagos Magma Chambers, in: Harpp, K.S.,  
910 Mittelstaedt, E., d’Ozouville, N., Graham, D.W. (Eds.), *Geophysical Monograph Series*. John  
911 Wiley & Sons, Inc, Hoboken, New Jersey, pp. 55–69.  
912 <https://doi.org/10.1002/9781118852538.ch5>

913 Geist, D.J., Fornari, D.J., Kurz, M.D., Harpp, K.S., Adam Soule, S., Perfit, M.R., Koleszar, A.M., 2006.  
914 Submarine Fernandina: Magmatism at the leading edge of the Galápagos hot spot.  
915 *Geochem. Geophys. Geosystems* 7, n/a-n/a. <https://doi.org/10.1029/2006GC001290>

916 Geist, D.J., White, W.M., McBirney, A.R., 1988. Plume-asthenosphere mixing beneath the Galapagos  
917 archipelago. *Nature* 333, 657–660. <https://doi.org/10.1038/333657a0>

918 Ghiorso, M.S., Gualda, G.A.R., 2015. An H<sub>2</sub>O–CO<sub>2</sub> mixed fluid saturation model compatible with  
919 rhyolite-MELTS. *Contrib. Mineral. Petrol.* 169, 53. [https://doi.org/10.1007/s00410-015-1141-](https://doi.org/10.1007/s00410-015-1141-8)  
920 [8](https://doi.org/10.1007/s00410-015-1141-8)

921 Gibson, S.A., Geist, D.G., Day, J.A., Dale, C.W., 2012. Short wavelength heterogeneity in the  
922 Galápagos plume: Evidence from compositionally diverse basalts on Isla Santiago. *Geochem.*  
923 *Geophys. Geosystems* 13. <https://doi.org/10.1029/2012GC004244>

924 Gibson, S.A., Richards, M.A., 2018. Delivery of deep-sourced, volatile-rich plume material to the  
925 global ridge system. *Earth Planet. Sci. Lett.* 499, 205–218.  
926 <https://doi.org/10.1016/j.epsl.2018.07.028>

927 Gleeson, M., Gibson, S., 2021. Insights into the nature of plume-ridge interaction and outflux of H<sub>2</sub>O  
928 from the Galápagos Spreading Centre. *Geochemistry, Geophysics, Geosystems*.  
929 e2020GC009560. <https://doi.org/10.1029/2020GC009560>

930 Gleeson, M., Soderman, C., Matthews, S., Cottaar, S. and Gibson, S., 2021. Geochemical constraints  
931 on the structure of the Earth’s deep mantle and the origin of the LLSVPs. *Geochemistry,*  
932 *Geophysics, Geosystems*, e2021GC009932. <https://doi.org/10.1029/2021GC009932>

933 Gleeson, M.L.M., Gibson, S.A., 2019. Crustal controls on apparent mantle pyroxenite signals in  
934 ocean-island basalts. *Geology*. <https://doi.org/10.1130/G45759.1>

935 Gleeson, Matthew L M, Gibson, S.A., Stock, M.J., 2020a. Upper mantle mush zones beneath low melt  
936 flux ocean island volcanoes: insights from Isla Floreana, Galápagos. *J. Petrol.* egaa094.  
937 <https://doi.org/10.1093/petrology/egaa094>

938 Gleeson, Matthew L.M., Gibson, S.A., Williams, H.M., 2020b. Novel insights from Fe-isotopes into the  
939 lithological heterogeneity of Ocean Island Basalts and plume-influenced MORBs. *Earth*  
940 *Planet. Sci. Lett.* 535, 116114. <https://doi.org/10.1016/j.epsl.2020.116114>

941 Graham, D.W., Hanan, B.B., Lupton, J.E., Hoernle, K., Werner, R., Christie, D.M., Sinton, J.M., 2014.  
942 Helium Isotope Variations and Mantle Plume-Spreading Ridge Interactions Along the  
943 Galápagos Spreading Center, in: Harpp, K.S., Mittelstaedt, E., d’Ozouville, N., Graham, D.W.  
944 (Eds.), *Geophysical Monograph Series*. John Wiley & Sons, Inc, Hoboken, New Jersey, pp.  
945 393–414. <https://doi.org/10.1002/9781118852538.ch18>

946 Hanyu, T., Shimizu, K., Ushikubo, T., Kimura, J.-I., Chang, Q., Hamada, M., Ito, M., Iwamori, H.,  
947 Ishikawa, T., 2019. Tiny droplets of ocean island basalts unveil Earth’s deep chlorine cycle.  
948 *Nat. Commun.* 10. <https://doi.org/10.1038/s41467-018-07955-8>

949 Harpp, K.S., Geist, D.J., 2018. The Evolution of Galápagos Volcanoes: An Alternative Perspective.  
950 Front. Earth Sci. 6. <https://doi.org/10.3389/feart.2018.00050>

951 Harpp, K.S., Geist, D.J., Koleszar, A.M., Christensen, B., Lyons, J., Sabga, M., Rollins, N., 2014. The  
952 Geology and Geochemistry of Isla Floreana, Galápagos: A Different Type of Late-Stage Ocean  
953 Island Volcanism, in: Harpp, K.S., Mittelstaedt, E., d'Ozouville, N., Graham, D.W. (Eds.),  
954 Geophysical Monograph Series. John Wiley & Sons, Inc, Hoboken, New Jersey, pp. 71–117.  
955 <https://doi.org/10.1002/9781118852538.ch6>

956 Harpp, K.S., Weis, D., 2020. Insights Into the Origins and Compositions of Mantle Plumes: A  
957 Comparison of Galápagos and Hawai'i. *Geochem. Geophys. Geosystems* 21.  
958 <https://doi.org/10.1029/2019GC008887>

959 Harpp, K.S., White, W.M., 2001. Tracing a mantle plume: Isotopic and trace element variations of  
960 Galápagos seamounts. *Geochem. Geophys. Geosystems* 2, n/a-n/a.  
961 <https://doi.org/10.1029/2000GC000137>

962 Hartley, M.E., Neave, D.A., Maclennan, J., Edmonds, M., Thordarson, T., 2015. Diffusive over-  
963 hydration of olivine-hosted melt inclusions. *Earth Planet. Sci. Lett.* 425, 168–178.  
964 <https://doi.org/10.1016/j.epsl.2015.06.008>

965 Hauri, E., Gaetani, G., Green, T., 2006. Partitioning of water during melting of the Earth's upper  
966 mantle at H<sub>2</sub>O-undersaturated conditions. *Earth Planet. Sci. Lett.* 248, 715–734.  
967 <https://doi.org/10.1016/j.epsl.2006.06.014>

968 Hirth, G., Kohlstedt, D., 2003. Rheology of the upper mantle and the mantle wedge: A view from the  
969 experimentalists, in: Eiler, J. (Ed.), *Geophysical Monograph Series*. American Geophysical  
970 Union, Washington, D. C., pp. 83–105. <https://doi.org/10.1029/138GM06>

971 Hirth, G., Kohlstedt, D.L., 1996. Water in the oceanic upper mantle: implications for rheology, melt  
972 extraction and the evolution of the lithosphere. *Earth Planet. Sci. Lett.* 144, 93–108.  
973 [https://doi.org/10.1016/0012-821X\(96\)00154-9](https://doi.org/10.1016/0012-821X(96)00154-9)

974 Hoernle, K., Werner, R., Morgan, J.P., Garbe-Schönberg, D., Bryce, J., Mrazek, J., 2000. Existence of  
975 complex spatial zonation in the Galápagos plume. *Geology* 28, 435.  
976 [https://doi.org/10.1130/0091-7613\(2000\)28<435:EOCSZ>2.0.CO;2](https://doi.org/10.1130/0091-7613(2000)28<435:EOCSZ>2.0.CO;2)

977 Hofmann, A.W., 1997. Mantle geochemistry: the message from oceanic volcanism. *Nature* 385, 219–  
978 229. <https://doi.org/10.1038/385219a0>

979 Hooft, E.E.E., Toomey, D.R., Solomon, S.C., 2003. Anomalously thin transition zone beneath the  
980 Galápagos hotspot. *Earth Planet. Sci. Lett.* 216, 55–64. [https://doi.org/10.1016/S0012-821X\(03\)00517-X](https://doi.org/10.1016/S0012-821X(03)00517-X)

982 Humphreys, M.C.S., Kearns, S.L., Blundy, J.D., 2006. SIMS investigation of electron-beam damage to  
983 hydrous, rhyolitic glasses: Implications for melt inclusion analysis. *Am. Mineral.* 91, 667–679.  
984 <https://doi.org/10.2138/am.2006.1936>

985 Iacono-Marziano, G., Morizet, Y., Le Trong, E., Gaillard, F., 2012. New experimental data and semi-  
986 empirical parameterization of H<sub>2</sub>O–CO<sub>2</sub> solubility in mafic melts. *Geochim. Cosmochim. Acta*  
987 97, 1–23. <https://doi.org/10.1016/j.gca.2012.08.035>

988 Iacovino, K., Matthews, S., Wieser, P., Moore, G., Bégué, F., 2020. VESICAL Part I: An open-source  
989 thermodynamic model engine for mixed volatile (H<sub>2</sub>O–CO<sub>2</sub>) solubility in silicate melts  
990 (preprint). *Earth Sciences*. <https://doi.org/10.31223/X5D606>

991 Ingle, S., Ito, G., Mahoney, J.J., Chazey, W., Sinton, J., Rotella, M., Christie, D.M., 2010. Mechanisms  
992 of geochemical and geophysical variations along the western Galápagos Spreading Center.  
993 *Geochem. Geophys. Geosystems* 11, n/a-n/a. <https://doi.org/10.1029/2009GC002694>

994 Jackson, M.G., Hart, S.R., Saal, A.E., Shimizu, N., Kurz, M.D., Blusztajn, J.S., Skovgaard, A.C., 2008.  
995 Globally elevated titanium, tantalum, and niobium (TITAN) in ocean island basalts with high  
996 <sup>34</sup>Si. *Geochem. Geophys. Geosystems* 9, n/a-n/a. <https://doi.org/10.1029/2007GC001876>

997 Jackson, M.G., Koga, K.T., Price, A., Konter, J.G., Koppers, A.A.P., Finlayson, V.A., Konrad, K., Hauri,  
998 E.H., Kylander-Clark, A., Kelley, K.A., Kendrick, M.A., 2015. Deeply dredged submarine HIMU  
999 glasses from the Tuvalu Islands, Polynesia: Implications for volatile budgets of recycled

1000 oceanic crust. *Geochem. Geophys. Geosystems* 16, 3210–3234.  
1001 <https://doi.org/10.1002/2015GC005966>

1002 Jarosewich, E., Nelen, J.A., Norberg, J.A., 1980. Reference Samples for Electron Microprobe  
1003 Analysis\*. *Geostand. Geoanalytical Res.* 4, 43–47. [https://doi.org/10.1111/j.1751-](https://doi.org/10.1111/j.1751-908X.1980.tb00273.x)  
1004 [908X.1980.tb00273.x](https://doi.org/10.1111/j.1751-908X.1980.tb00273.x)

1005 Katz, R.F., Spiegelman, M., Langmuir, C.H., 2003. A new parameterization of hydrous mantle melting.  
1006 *Geochem. Geophys. Geosystems* 4, n/a-n/a. <https://doi.org/10.1029/2002GC000433>

1007 Kendrick, M.A., Hémond, C., Kamenetsky, V.S., Danyushevsky, L., Devey, C.W., Rodemann, T.,  
1008 Jackson, M.G., Perfit, M.R., 2017. Seawater cycled throughout Earth's mantle in partially  
1009 serpentinized lithosphere. *Nat. Geosci.* 10, 222–228. <https://doi.org/10.1038/ngeo2902>

1010 Kendrick, M.A., Jackson, M.G., Hauri, E.H., Phillips, D., 2015. The halogen (F, Cl, Br, I) and H<sub>2</sub>O  
1011 systematics of Samoan lavas: Assimilated-seawater, EM2 and high-<sup>3</sup>He/<sup>4</sup>He components.  
1012 *Earth Planet. Sci. Lett.* 410, 197–209. <https://doi.org/10.1016/j.epsl.2014.11.026>

1013 Kendrick, M.A., Jackson, M.G., Kent, A.J.R., Hauri, E.H., Wallace, P.J., Woodhead, J., 2014. Contrasting  
1014 behaviours of CO<sub>2</sub>, S, H<sub>2</sub>O and halogens (F, Cl, Br, and I) in enriched-mantle melts from  
1015 Pitcairn and Society seamounts. *Chem. Geol.* 370, 69–81.  
1016 <https://doi.org/10.1016/j.chemgeo.2014.01.019>

1017 Koleszar, A.M., Saal, A.E., Hauri, E.H., Nagle, A.N., Liang, Y., Kurz, M.D., 2009. The volatile contents of  
1018 the Galapagos plume; evidence for H<sub>2</sub>O and F open system behavior in melt inclusions.  
1019 *Earth Planet. Sci. Lett.* 287, 442–452. <https://doi.org/10.1016/j.epsl.2009.08.029>

1020 Kumamoto, K.M., Warren, J.M., Hauri, E.H., 2017. New SIMS reference materials for measuring  
1021 water in upper mantle minerals. *Am. Mineral.* 102, 537–547. [https://doi.org/10.2138/am-](https://doi.org/10.2138/am-2017-5863CCBYNCND)  
1022 [2017-5863CCBYNCND](https://doi.org/10.2138/am-2017-5863CCBYNCND)

1023 Kurz, M.D., Curtice, J., Fornari, D., Geist, D., Moreira, M., 2009. Primitive neon from the center of the  
1024 Galápagos hotspot. *Earth Planet. Sci. Lett.* 286, 23–34.  
1025 <https://doi.org/10.1016/j.epsl.2009.06.008>

1026 Kurz, M.D., Geist, D., 1999. Dynamics of the Galapagos hotspot from helium isotope geochemistry.  
1027 *Geochim. Cosmochim. Acta* 63, 4139–4156. [https://doi.org/10.1016/S0016-7037\(99\)00314-](https://doi.org/10.1016/S0016-7037(99)00314-2)  
1028 [2](https://doi.org/10.1016/S0016-7037(99)00314-2)

1029 Lambert, S., Baker, M.B., Stolper, E.M., 2016. The role of pyroxenite in basalt genesis: Melt-PX, a  
1030 melting parameterization for mantle pyroxenites between 0.9 and 5 GPa: Melt-PX:  
1031 Pyroxenite Melting Model. *J. Geophys. Res. Solid Earth* 121, 5708–5735.  
1032 <https://doi.org/10.1002/2015JB012762>

1033 Lassiter, J.C., Hauri, E.H., Nikogosian, I.K., Barszczus, H.G., 2002. Chlorine–potassium variations in melt  
1034 inclusions from Raivavae and Rapa, Austral Islands: constraints on chlorine recycling in the  
1035 mantle and evidence for brine-induced melting of oceanic crust. *Earth Planet. Sci. Lett.* 202,  
1036 525–540. [https://doi.org/10.1016/S0012-821X\(02\)00826-9](https://doi.org/10.1016/S0012-821X(02)00826-9)

1037 Le Roux, P., Shirey, S., Hauri, E., Perfit, M., Bender, J., 2006. The effects of variable sources,  
1038 processes and contaminants on the composition of northern EPR MORB (8–10°N and 12–  
1039 14°N): Evidence from volatiles (H<sub>2</sub>O, CO<sub>2</sub>, S) and halogens (F, Cl). *Earth Planet. Sci. Lett.* 251,  
1040 209–231. <https://doi.org/10.1016/j.epsl.2006.09.012>

1041 Lissenberg, C.J., MacLeod, C.J., 2016. A Reactive Porous Flow Control on Mid-ocean Ridge Magmatic  
1042 Evolution. *J. Petrol.* 57, 2195–2220. <https://doi.org/10.1093/petrology/egw074>

1043 Lloyd, A.S., Ferriss, E., Ruprecht, P., Hauri, E.H., Jicha, B.R., Plank, T., 2016. An Assessment of  
1044 Clinopyroxene as a Recorder of Magmatic Water and Magma Ascent Rate. *J. Petrol.* 57,  
1045 1865–1886. <https://doi.org/10.1093/petrology/egw058>

1046 Lloyd, A.S., Ruprecht, P., Hauri, E.H., Rose, W., Gonnermann, H.M., Plank, T., 2014. NanoSIMS results  
1047 from olivine-hosted melt embayments: Magma ascent rate during explosive basaltic  
1048 eruptions. *J. Volcanol. Geotherm. Res.* 283, 1–18.  
1049 <https://doi.org/10.1016/j.jvolgeores.2014.06.002>

1050 Lyons, J., Geist, D., Harpp, K., Diefenbach, B., Olin, P., Vervoort, J., 2007. Crustal growth by magmatic  
1051 overplating in the Galápagos. *Geology* 35, 511. <https://doi.org/10.1130/G23044A.1>

1052 Maclennan, J., 2017. Bubble formation and decrepitation control the CO<sub>2</sub> content of olivine-hosted  
1053 melt inclusions. *Geochem. Geophys. Geosystems* 18, 597–616.  
1054 <https://doi.org/10.1002/2016GC006633>

1055 Maclennan, J., 2008. Concurrent Mixing and Cooling of Melts under Iceland. *J. Petrol.* 49, 1931–  
1056 1953. <https://doi.org/10.1093/petrology/egn052>

1057 Marks, M.A.W., Kendrick, M.A., Eby, G.N., Zack, T., Wenzel, T., 2017. The F, Cl, Br and I Contents of  
1058 Reference Glasses BHVO-2G, BIR-1G, BCR-2G, GSD-1G, GSE-1G, NIST SRM 610 and NIST SRM  
1059 612. *Geostand. Geoanalytical Res.* 41, 107–122. <https://doi.org/10.1111/ggr.12128>

1060 Métrich, N., Zanon, V., Créon, L., Hildenbrand, A., Moreira, M., Marques, F.O., 2014. Is the ‘Azores  
1061 Hotspot’ a Wetspot? Insights from the Geochemistry of Fluid and Melt Inclusions in Olivine  
1062 of Pico Basalts. *J. Petrol.* 55, 377–393. <https://doi.org/10.1093/petrology/egt071>

1063 Michael, P., 1995. Regionally distinctive sources of depleted MORB: Evidence from trace elements  
1064 and H<sub>2</sub>O. *Earth Planet. Sci. Lett.* 131, 301–320. [https://doi.org/10.1016/0012-  
1065 821X\(95\)00023-6](https://doi.org/10.1016/0012-821X(95)00023-6)

1066 Michael, P.J., Cornell, W.C., 1998. Influence of spreading rate and magma supply on crystallization  
1067 and assimilation beneath mid-ocean ridges: Evidence from chlorine and major element  
1068 chemistry of mid-ocean ridge basalts. *J. Geophys. Res. Solid Earth* 103, 18325–18356.  
1069 <https://doi.org/10.1029/98JB00791>

1070 Miller, W.G.R., Maclennan, J., Shorttle, O., Gaetani, G.A., Le Roux, V., Klein, F., 2019. Estimating the  
1071 carbon content of the deep mantle with Icelandic melt inclusions. *Earth Planet. Sci. Lett.* 523,  
1072 115699. <https://doi.org/10.1016/j.epsl.2019.07.002>

1073 Nazzareni, S., Barbarossa, V., Skogby, H., Zanon, V., Petrelli, M., 2020. Magma water content of Pico  
1074 Volcano (Azores Islands, Portugal): a clinopyroxene perspective. *Contrib. Mineral. Petrol.*  
1075 175, 87. <https://doi.org/10.1007/s00410-020-01728-7>

1076 Novella, D., Frost, D.J., Hauri, E.H., Bureau, H., Raepsaet, C., Roberge, M., 2014. The distribution of  
1077 H<sub>2</sub>O between silicate melt and nominally anhydrous peridotite and the onset of hydrous  
1078 melting in the deep upper mantle. *Earth Planet. Sci. Lett.* 400, 1–13.  
1079 <https://doi.org/10.1016/j.epsl.2014.05.006>

1080 O’Leary, J.A., Gaetani, G.A., Hauri, E.H., 2010. The effect of tetrahedral Al<sup>3+</sup> on the partitioning of  
1081 water between clinopyroxene and silicate melt. *Earth Planet. Sci. Lett.* 297, 111–120.  
1082 <https://doi.org/10.1016/j.epsl.2010.06.011>

1083 Peterson, M.E., Saal, A.E., Kurz, M.D., Hauri, E.H., Blusztajn, J.S., Harpp, K.S., Werner, R., Geist, D.J.,  
1084 2017. Submarine Basaltic Glasses from the Galapagos Archipelago: Determining the Volatile  
1085 Budget of the Mantle Plume. *J. Petrol.* 58, 1419–1450.  
1086 <https://doi.org/10.1093/petrology/egx059>

1087 Poland, M.P., 2014. Contrasting Volcanism in Hawai’i and the Galápagos, in: Harpp, K.S.,  
1088 Mittelstaedt, E., d’Ozouville, N., Graham, D.W. (Eds.), *Geophysical Monograph Series*. John  
1089 Wiley & Sons, Inc, Hoboken, New Jersey, pp. 5–26.  
1090 <https://doi.org/10.1002/9781118852538.ch2>

1091 Roeder, P.L., Emslie, R.F., 1970. Olivine-liquid equilibrium. *Contr. Miner. Pet.* 29, 275–289.  
1092 <https://doi.org/10.1007/BF00371276>

1093 Rosenthal, A., Yaxley, G.M., Green, D.H., Hermann, J., Kovács, I., Spandler, C., 2015. Continuous  
1094 eclogite melting and variable refertilisation in upwelling heterogeneous mantle. *Sci. Rep.* 4.  
1095 <https://doi.org/10.1038/srep06099>

1096 Rudge, J.F., Maclennan, J., Stracke, A., 2013. The geochemical consequences of mixing melts from a  
1097 heterogeneous mantle. *Geochim. Cosmochim. Acta* 114, 112–143.  
1098 <https://doi.org/10.1016/j.gca.2013.03.042>



1099 Saal, A., Kurz, M., Hart, S., Blusztajn, J., Blicherttoft, J., Liang, Y., Geist, D., 2007. The role of  
1100 lithospheric gabbros on the composition of Galapagos lavas. *Earth Planet. Sci. Lett.* 257,  
1101 391–406. <https://doi.org/10.1016/j.epsl.2007.02.040>

1102 Saal, A.E., Hauri, E.H., Langmuir, C.H., Perfit, M.R., 2002. Vapour undersaturation in primitive mid-  
1103 ocean-ridge basalt and the volatile content of Earth's upper mantle. *Nature* 419, 451–455.  
1104 <https://doi.org/10.1038/nature01073>

1105 Sheather, S.J., Jones, M.C., 1991. A Reliable Data-Based Bandwidth Selection Method for Kernel  
1106 Density Estimation. *J. R. Stat. Soc. Ser. B Methodol.* 53, 683–690.  
1107 <https://doi.org/10.1111/j.2517-6161.1991.tb01857.x>

1108 Shimizu, K., Saal, A.E., Myers, C.E., Nagle, A.N., Hauri, E.H., Forsyth, D.W., Kamenetsky, V.S., Niu, Y.,  
1109 2016. Two-component mantle melting-mixing model for the generation of mid-ocean ridge  
1110 basalts: Implications for the volatile content of the Pacific upper mantle. *Geochim.*  
1111 *Cosmochim. Acta* 176, 44–80. <https://doi.org/10.1016/j.gca.2015.10.033>

1112 Shishkina, T.A., Botcharnikov, R.E., Holtz, F., Almeev, R.R., Jazwa, A.M., Jakubiak, A.A., 2014.  
1113 Compositional and pressure effects on the solubility of H<sub>2</sub>O and CO<sub>2</sub> in mafic melts. *Chem.*  
1114 *Geol.* 388, 112–129. <https://doi.org/10.1016/j.chemgeo.2014.09.001>

1115 Shishkina, T.A., Botcharnikov, R.E., Holtz, F., Almeev, R.R., Portnyagin, M.V., 2010. Solubility of H<sub>2</sub>O-  
1116 and CO<sub>2</sub>-bearing fluids in tholeiitic basalts at pressures up to 500MPa. *Chem. Geol.* 277,  
1117 115–125. <https://doi.org/10.1016/j.chemgeo.2010.07.014>

1118 Sides, I.R., Edmonds, M., MacLennan, J., Swanson, D.A., Houghton, B.F., 2014. Eruption style at  
1119 Kīlauea Volcano in Hawai'i linked to primary melt composition. *Nat. Geosci.* 7, 464–469.  
1120 <https://doi.org/10.1038/ngeo2140>

1121 Steele-Macinnis, M., Esposito, R., Bodnar, R.J., 2011. Thermodynamic Model for the Effect of Post-  
1122 entrapment Crystallization on the H<sub>2</sub>O-CO<sub>2</sub> Systematics of Vapor-saturated, Silicate Melt  
1123 Inclusions. *J. Petrol.* 52, 2461–2482. <https://doi.org/10.1093/petrology/egr052>

1124 Stock, M.J., Bagnardi, M., Neave, D.A., MacLennan, J., Bernard, B., Buisman, I., Gleeson, M.L.M.,  
1125 Geist, D., 2018. Integrated Petrological and Geophysical Constraints on Magma System  
1126 Architecture in the Western Galápagos Archipelago: Insights From Wolf Volcano. *Geochem.*  
1127 *Geophys. Geosystems* 19, 4722–4743. <https://doi.org/10.1029/2018GC007936>

1128 Stock, M.J., Geist, D., Neave, D.A., Gleeson, M.L.M., Bernard, B., Howard, K.A., Buisman, I.,  
1129 MacLennan, J., 2020. Cryptic evolved melts beneath monotonous basaltic shield volcanoes in  
1130 the Galápagos Archipelago. *Nat. Commun.* 11, 3767. <https://doi.org/10.1038/s41467-020-17590-x>

1131

1132 Stock, M.J., Humphreys, M.C.S., Smith, V.C., Isaia, R., Pyle, D.M., 2016. Late-stage volatile saturation  
1133 as a potential trigger for explosive volcanic eruptions. *Nat. Geosci.* 9, 249–254.  
1134 <https://doi.org/10.1038/ngeo2639>

1135 Sun, S. -s., McDonough, W.F., 1989. Chemical and isotopic systematics of oceanic basalts:  
1136 implications for mantle composition and processes. *Geol. Soc. Lond. Spec. Publ.* 42, 313–  
1137 345. <https://doi.org/10.1144/GSL.SP.1989.042.01.19>

1138 Turner, M., Turner, S., Mironov, N., Portnyagin, M., Hoernle, K., 2017. Can magmatic water contents  
1139 be estimated from clinopyroxene phenocrysts in some lavas? A case study with implications  
1140 for the origin of the Azores Islands. *Chem. Geol.* 466, 436–445.  
1141 <https://doi.org/10.1016/j.chemgeo.2017.06.032>

1142 Ubide, T., Galé, C., Larrea, P., Arranz, E., Lago, M., 2014. Antecrysts and their effect on rock  
1143 compositions: The Cretaceous lamprophyre suite in the Catalonian Coastal Ranges (NE  
1144 Spain) 20.

1145 Vasconez, F., Ramón, P., Hernandez, S., Hidalgo, S., Bernard, B., Ruiz, M., Alvarado, A., La Femina, P.,  
1146 Ruiz, G., 2018. The different characteristics of the recent eruptions of Fernandina and Sierra  
1147 Negra volcanoes (Galápagos, Ecuador). *Volcanica* 1, 127–133.  
1148 <https://doi.org/10.30909/vol.01.02.127133>

1149 Vidito, C., Herzberg, C., Gazel, E., Geist, D., Harpp, K., 2013. Lithological structure of the Galápagos  
1150 Plume: Lithological Structure Galpagos Plume. *Geochem. Geophys. Geosystems* 14, 4214–  
1151 4240. <https://doi.org/10.1002/ggge.20270>

1152 Villagómez, D.R., Toomey, D.R., Geist, D.J., Hooft, E.E.E., Solomon, S.C., 2014. Mantle flow and  
1153 multistage melting beneath the Galápagos hotspot revealed by seismic imaging. *Nat. Geosci.*  
1154 7, 151–156. <https://doi.org/10.1038/ngeo2062>

1155 Wade, J.A., Plank, T., Hauri, E.H., Kelley, K.A., Roggensack, K., Zimmer, M., 2008. Prediction of  
1156 magmatic water contents via measurement of H<sub>2</sub>O in clinopyroxene phenocrysts. *Geology*  
1157 36, 799. <https://doi.org/10.1130/G24964A.1>

1158 Weiss, Y., Class, C., Goldstein, S.L., Hanyu, T., 2016. Key new pieces of the HIMU puzzle from olivines  
1159 and diamond inclusions. *Nature* 537, 666–670. <https://doi.org/10.1038/nature19113>

1160 White, W.M., 2010. Oceanic Island Basalts and Mantle Plumes: The Geochemical Perspective. *Annu.*  
1161 *Rev. Earth Planet. Sci.* 38, 133–160. <https://doi.org/10.1146/annurev-earth-040809-152450>

1162 White, W.M., McBirney, A.R., Duncan, R.A., 1993. Petrology and geochemistry of the Galápagos  
1163 Islands: Portrait of a pathological mantle plume. *J. Geophys. Res. Solid Earth* 98, 19533–  
1164 19563. <https://doi.org/10.1029/93JB02018>

1165 Wieser, P., Iacovino, K., Matthews, S., Moore, G., Allison, C., 2021. VESlcal Part II: A critical approach  
1166 to volatile solubility modelling using an open-source Python3 engine (preprint). *Earth*  
1167 *Sciences*. <https://doi.org/10.31223/X5K03T>

1168 Wieser, P.E., Edmonds, M., Maclennan, J., Jenner, F.E., Kunz, B.E., 2019. Crystal scavenging from  
1169 mush piles recorded by melt inclusions. *Nat. Commun.* 10, 5797.  
1170 <https://doi.org/10.1038/s41467-019-13518-2>

1171 Wieser, P.E., Lamadrid, H., Maclennan, J., Edmonds, M., Matthews, S., Iacovino, K., Jenner, F.E.,  
1172 Gansecki, C., Trusdell, F., Lee, R.L., Ilyinskaya, E., 2020. Reconstructing Magma Storage  
1173 Depths for the 2018 Kīlauea Eruption from Melt inclusion CO<sub>2</sub> Contents: The Importance of  
1174 Vapor Bubbles. *Geochem. Geophys. Geosystems*. <https://doi.org/10.1029/2020GC009364>

1175 Witham, F., Blundy, J., Kohn, S.C., Lesne, P., Dixon, J., Churakov, S.V., Botcharnikov, R., 2012. SolEx: A  
1176 model for mixed COHSCI-volatile solubilities and exsolved gas compositions in basalt.  
1177 *Comput. Geosci.* 45, 87–97. <https://doi.org/10.1016/j.cageo.2011.09.021>

1178 Wood, B.J., Blundy, J.D., 1997. A predictive model for rare earth element partitioning between  
1179 clinopyroxene and anhydrous silicate melt. *Contrib. Mineral. Petrol.* 129, 166–181.  
1180 <https://doi.org/10.1007/s004100050330>

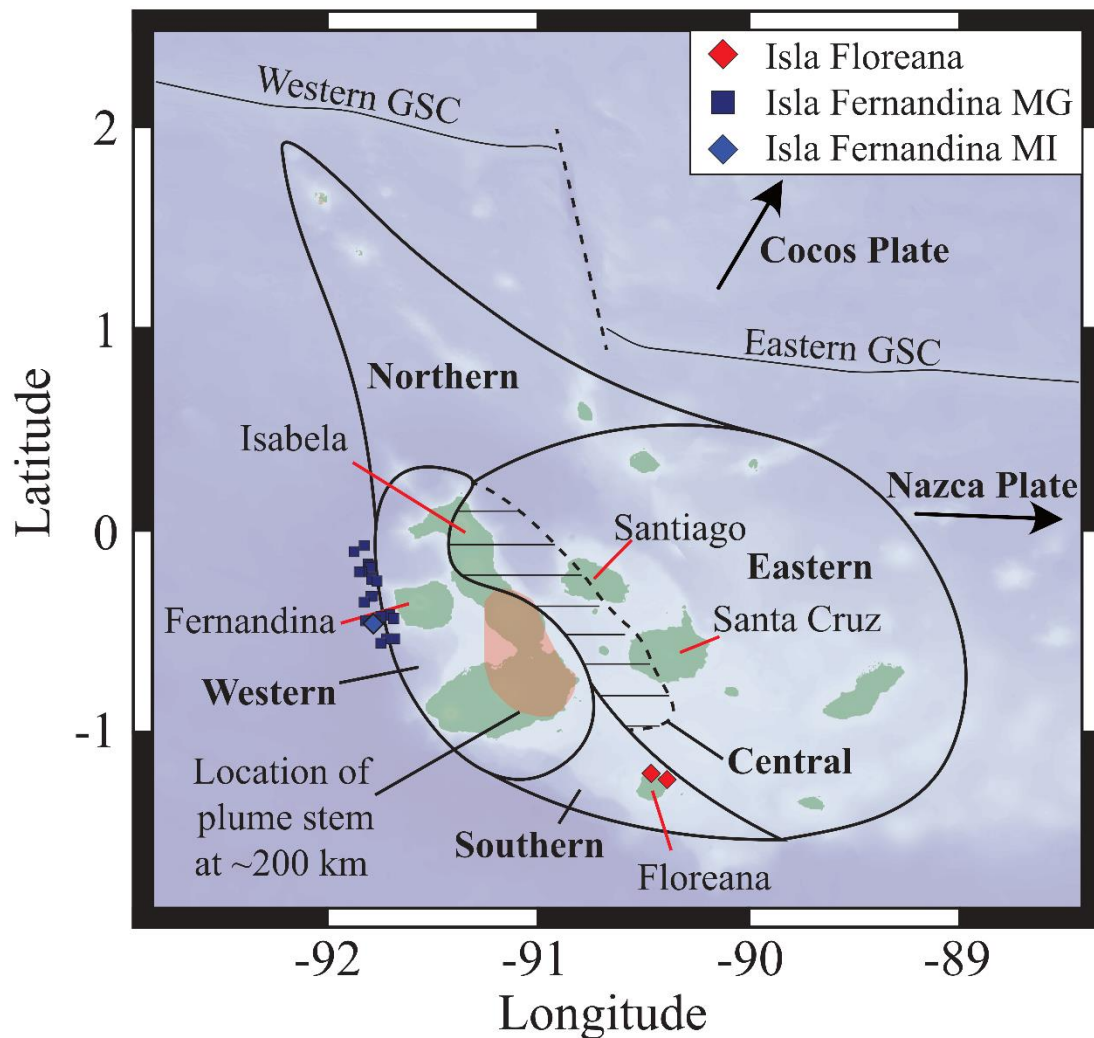
1181 Workman, R.K., Hauri, E., Hart, S.R., Wang, J., Blusztajn, J., 2006. Volatile and trace elements in  
1182 basaltic glasses from Samoa: Implications for water distribution in the mantle. *Earth Planet.*  
1183 *Sci. Lett.* 241, 932–951. <https://doi.org/10.1016/j.epsl.2005.10.028>

1184 Zhang, Y., Ni, H., 2010. Diffusion of H, C, and O Components in Silicate Melts. *Rev. Mineral.*  
1185 *Geochem.* 72, 171–225. <https://doi.org/10.2138/rmg.2010.72.5>

1186 Zhang, Y., Ni, H., Chen, Y., 2010. Diffusion Data in Silicate Melts. *Rev. Mineral. Geochem.* 72, 311–  
1187 408. <https://doi.org/10.2138/rmg.2010.72.8>

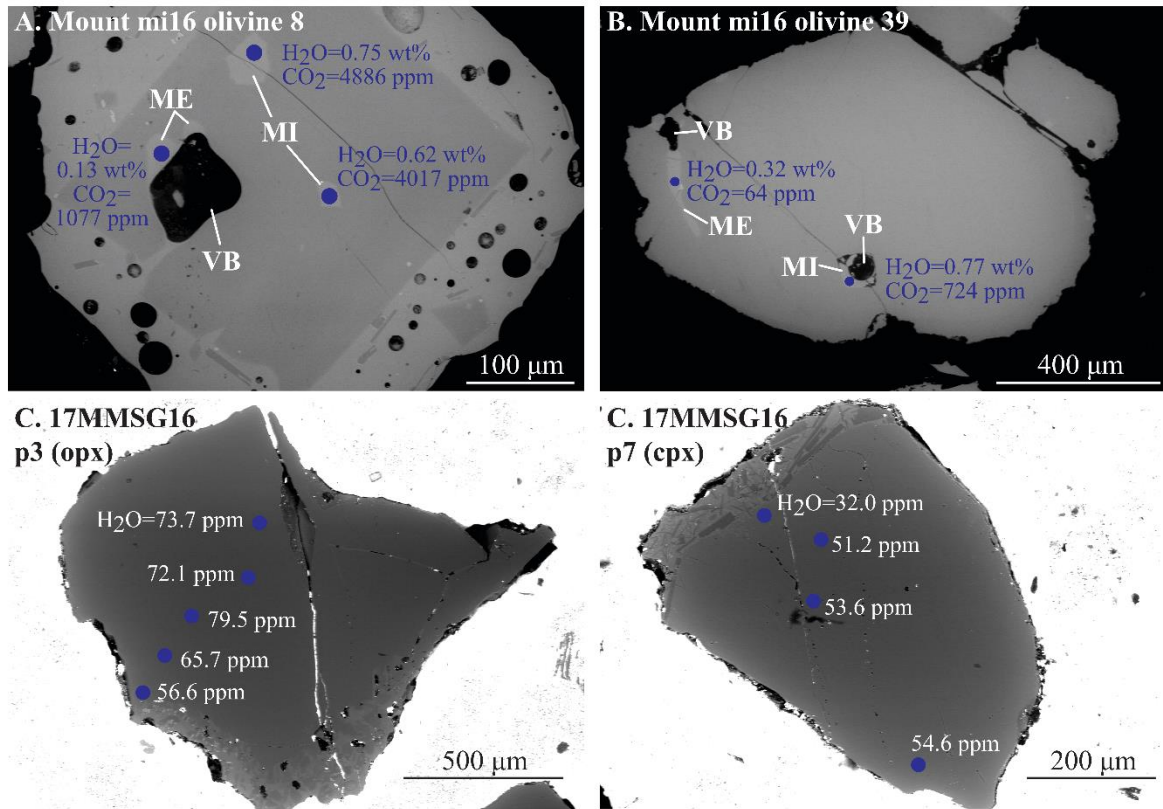
1188 Zindler, A., Hart, S., 1986. Helium: problematic primordial signals. *Earth Planet. Sci. Lett.* 79, 1–8.  
1189 [https://doi.org/10.1016/0012-821X\(86\)90034-8](https://doi.org/10.1016/0012-821X(86)90034-8)

1190



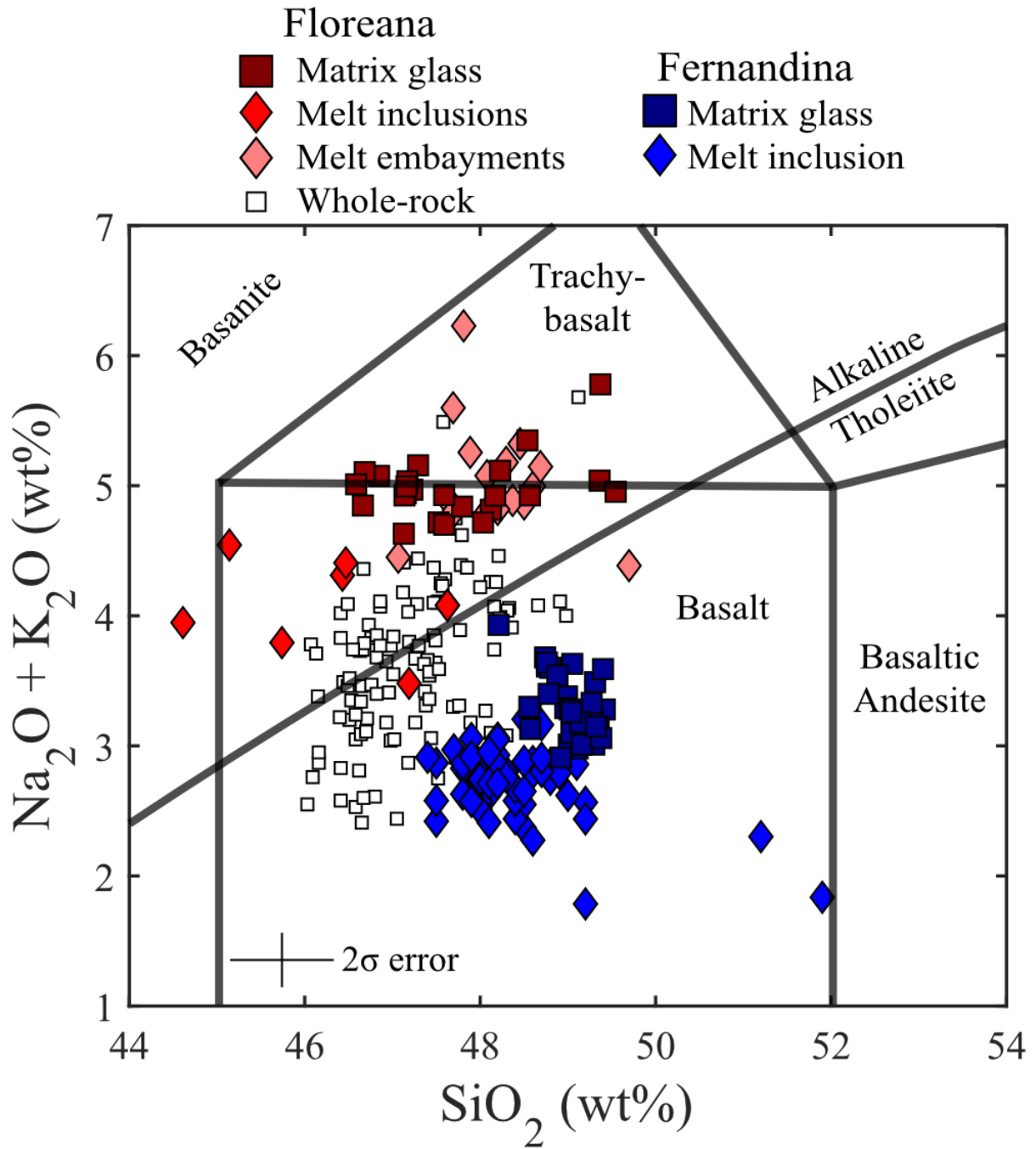
1192

1193 **Figure 1** – Map of the Galápagos Archipelago. The approximate location of the various isotopic  
 1194 components expressed in the composition of the Galápagos basalts are taken from Hoernle et al.  
 1195 (2000) and Gleeson et al. (2020b). The location of the mantle plume at ~200 km depth (from  
 1196 Villagómez et al., 2014) together with the location of samples used in this study (from Koleszar et al.  
 1197 (2009), Peterson et al. (2017) and Gleeson et al. (2020a)) are also shown.



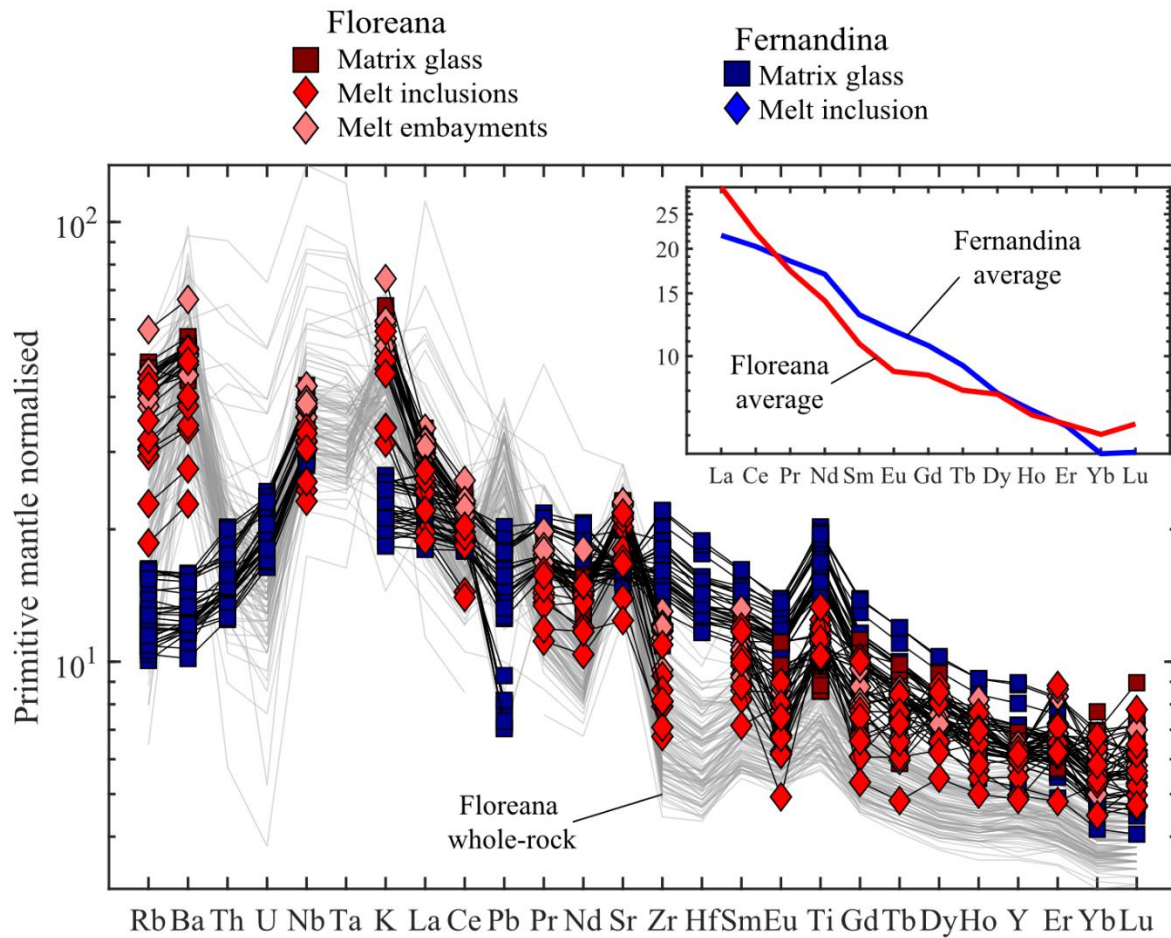
1198

1199 **Figure 2** – SEM images of olivine-hosted melt inclusions and orthopyroxene and clinopyroxene grains  
 1200 mounted in indium. **A.** Small olivine crystal (~400 μm across) with 2 melt inclusions that both  
 1201 preserve relatively high CO<sub>2</sub> contents. A small embayment on the edge of this crystal has low H<sub>2</sub>O  
 1202 contents consistent with degassing and diffusive loss of H<sub>2</sub>O from this melt. **B.** A melt inclusion with  
 1203 a large, possibly co-entrapped, vapour bubble in a larger olivine crystal. Also present in this crystal is  
 1204 a relatively long (~200 μm) melt embayment that preserves high melt H<sub>2</sub>O contents (~0.33 wt%). **C.**  
 1205 H<sub>2</sub>O content of an orthopyroxene crystal from scoria sample 17MMSG16. The H<sub>2</sub>O content in the  
 1206 core of this crystal is relatively constant, but the rim analysis returns notably lower H<sub>2</sub>O contents  
 1207 than the core analyses. **D.** A similar spatial relationship is seen in some of the clinopyroxene crystals  
 1208 from Floreana, where the rim analysis returns slightly lower H<sub>2</sub>O contents than the core analyses. MI  
 1209 – melt inclusion; ME – melt embayment; VB – vapour bubble.



1210

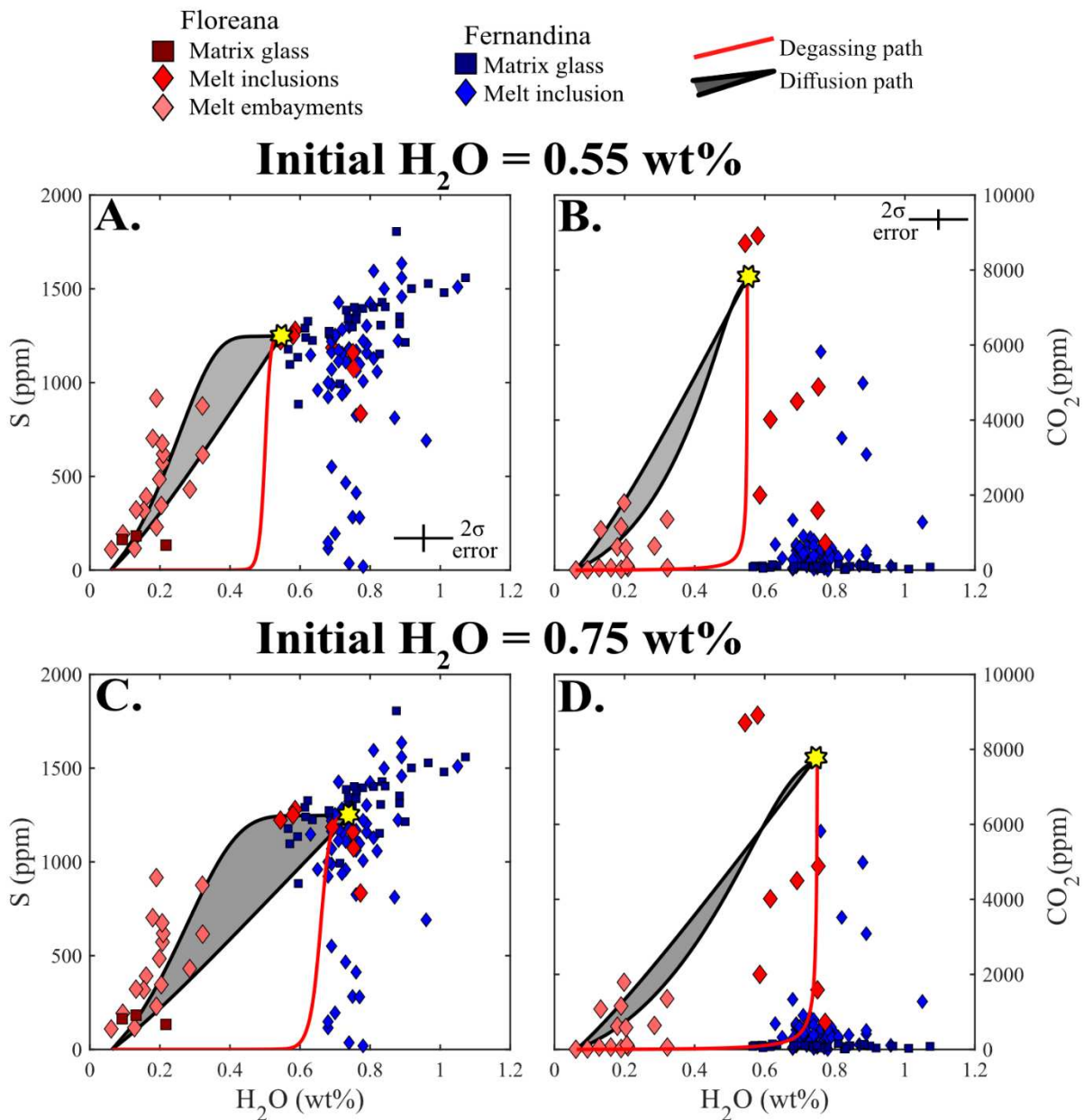
1211 **Figure 3** – Total alkalis versus silica plot of the Floreana melt inclusions, melt embayments and  
 1212 matrix glasses (Irvine and Baragar, 1971). The  $\text{Na}_2\text{O} + \text{K}_2\text{O}$  content of most Floreana matrix glasses,  
 1213 and the majority of melt inclusions and melt embayments straddle the divide between basalts and  
 1214 trachy-basalts. Floreana matrix glass data is taken from Gleeson et al. (2020a) and the whole-rock  
 1215 data is taken from Harpp et al. (2014). Data from Isla Fernandina is taken from Koleszar et al. (2009)  
 1216 and Peterson et al. (2017).



1217

1218 **Figure 4** – Trace element composition of the Fernandina and Floreana basalts. The Floreana basalts  
 1219 contain high concentrations of fluid-mobile trace elements (such as Ba; Harpp et al., 2014). This  
 1220 signature is observed in both our new melt inclusion and matrix glass data as well as published  
 1221 whole-rock data (Harpp et al., 2014). The Floreana basalts display concave-up rare earth element  
 1222 (REE) signatures, with steep light-to-middle REE slopes and shallow middle-to-heavy REE slopes  
 1223 (inset). Data from Isla Fernandina is from Koleszar et al. (2009) and Peterson et al. (2017). Primitive  
 1224 mantle values are taken from Sun and McDonough (1989).





1225

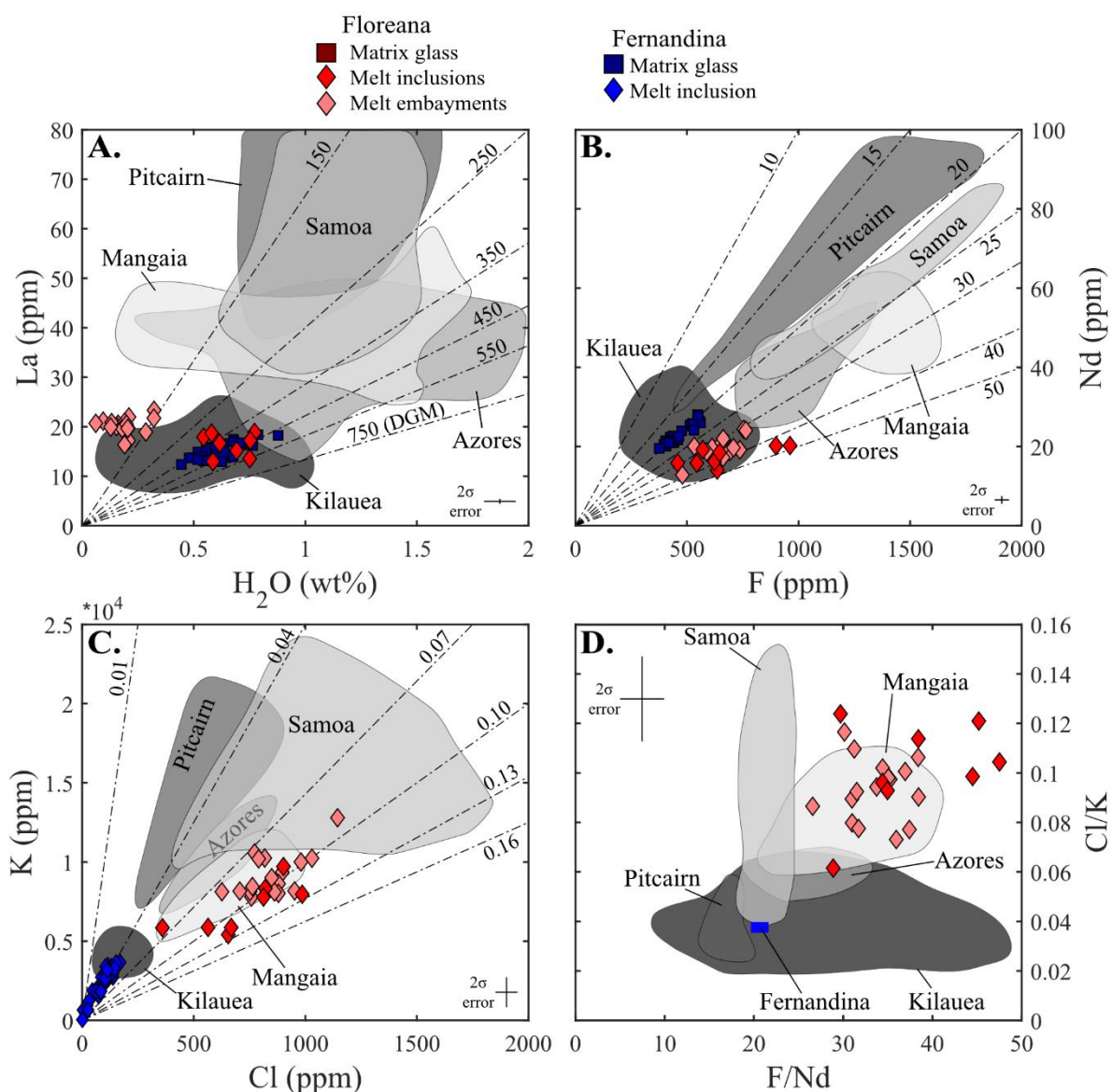
1226 **Figure 5** – Volatile systematics of the Floreana melt inclusions and melt embayments. Grey shaded  
 1227 areas in all plots reveal the range of compositions that are observed in modelled embayments  
 1228 following combined decompression – diffusion models. Results are shown for all models that initiate  
 1229 at 750 MPa with decompression rates between 0.005 and 0.5 MPa/s. The H<sub>2</sub>O vs S systematics of the  
 1230 Floreana melt embayments can be matched by models that have initial melt embayment H<sub>2</sub>O  
 1231 contents between 0.55 wt% (**A.**, **B.**) and 0.75 wt% (**C.**, **D.**). Fernandina data from Koleszar et al. (2009)  
 1232 and Peterson et al. (2017).



1233

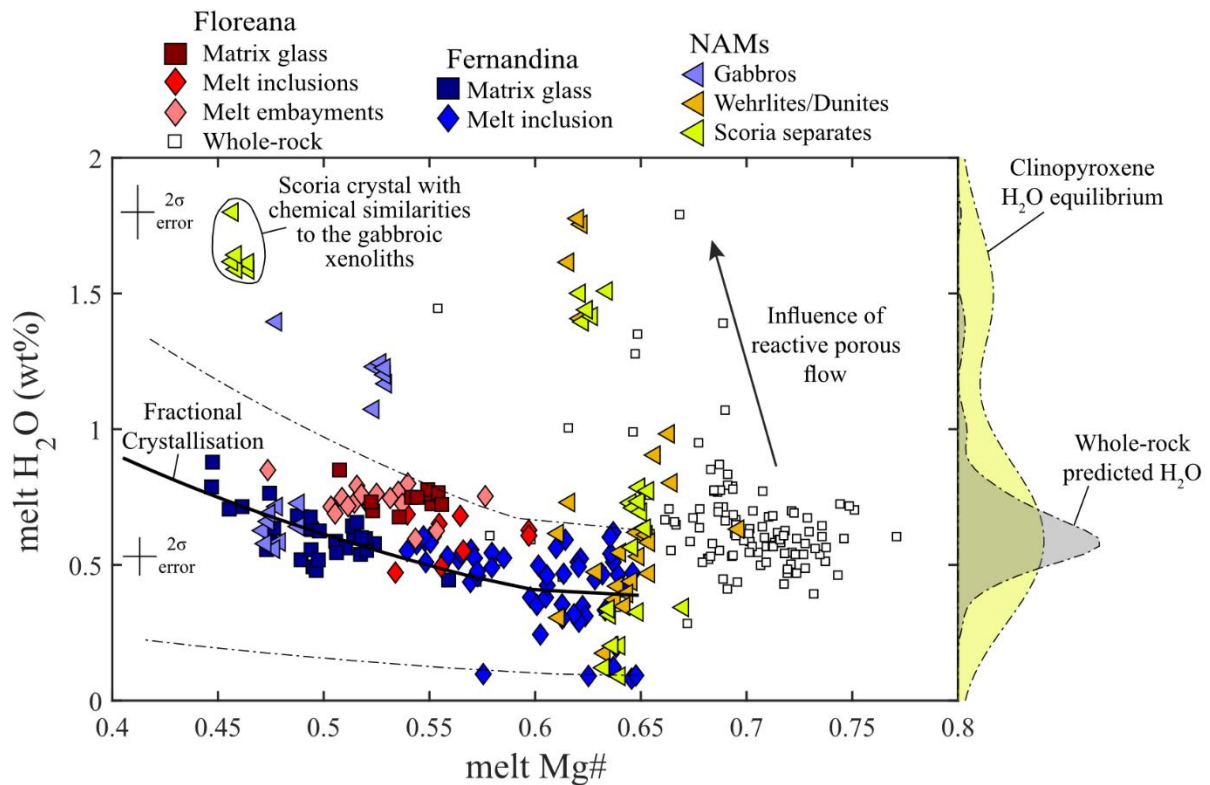
1234 **Figure 6** – Correlation matrix calculated from the trace and volatile element concentrations of the  
 1235 Floreana melt inclusions and melt embayments. The colour of each square is controlled by the  
 1236 correlation coefficient of the two elements of interest (red = positive correlation; blue = negative  
 1237 correlation). The correlation coefficient of each square is shown, white lettering indicates that the  
 1238 correlation is significant at the 95% confidence interval..





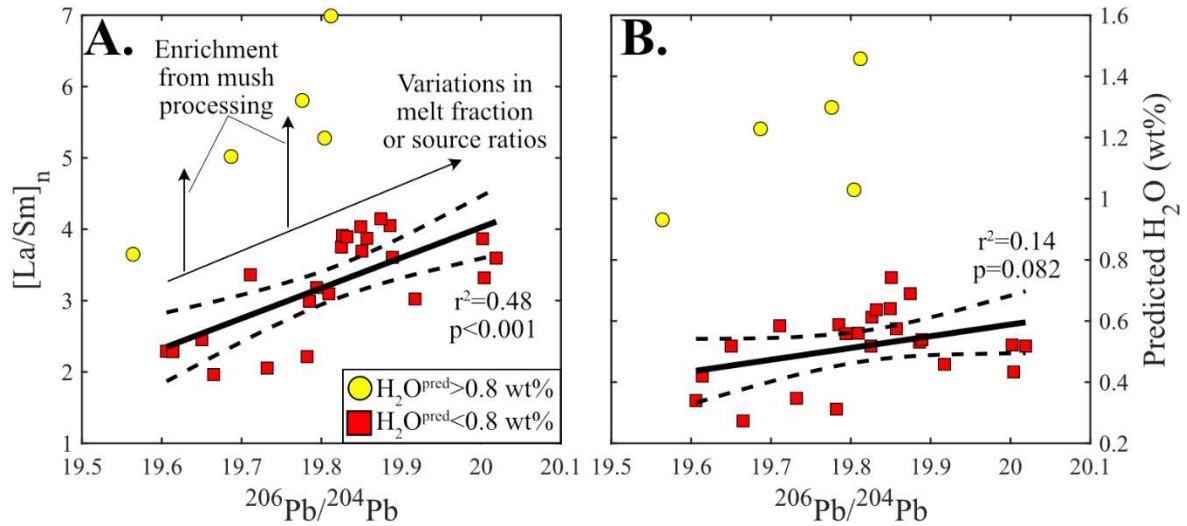
1239

1240 **Figure 7** – Volatile vs non-volatile trace element systematics of the Floreana and Fernandina basalts.  
 1241 Lines of constant volatile to non-volatile trace element ratios (i.e. constant H<sub>2</sub>O/La, F/Nd, or Cl/K) are  
 1242 displayed in panels A. to C.. **A.** There is a large range in the H<sub>2</sub>O contents of the Floreana melt  
 1243 inclusions and melt embayments, but only a narrow range of La contents. DGM refers to the  
 1244 Depleted Galápagos Mantle and the H<sub>2</sub>O/La ratio of this component is constrained in Gleeson and  
 1245 Gibson (2021). **B.** F vs Nd, the F content of the Floreana basalts are regularly higher than the F  
 1246 contents of basalts from Fernandina at an equivalent Nd concentration (data from Peterson et al.,  
 1247 2017). **C.** Cl vs K, the Floreana basalts have consistently higher Cl and K contents than melt inclusions  
 1248 from Fernandina (Koleszar et al., 2009). **D.** The high F/Nd and Cl/K ratios of the Floreana melt  
 1249 inclusions and melt embayments is rarely observed in ocean island basalts. Data presented in this  
 1250 figure from Cabral et al. (2014); Kendrick et al. (2014); Koleszar et al. (2009); Métrich et al. (2014);  
 1251 Peterson et al. (2017); Sides et al. (2014); Workman et al. (2006) and this study.



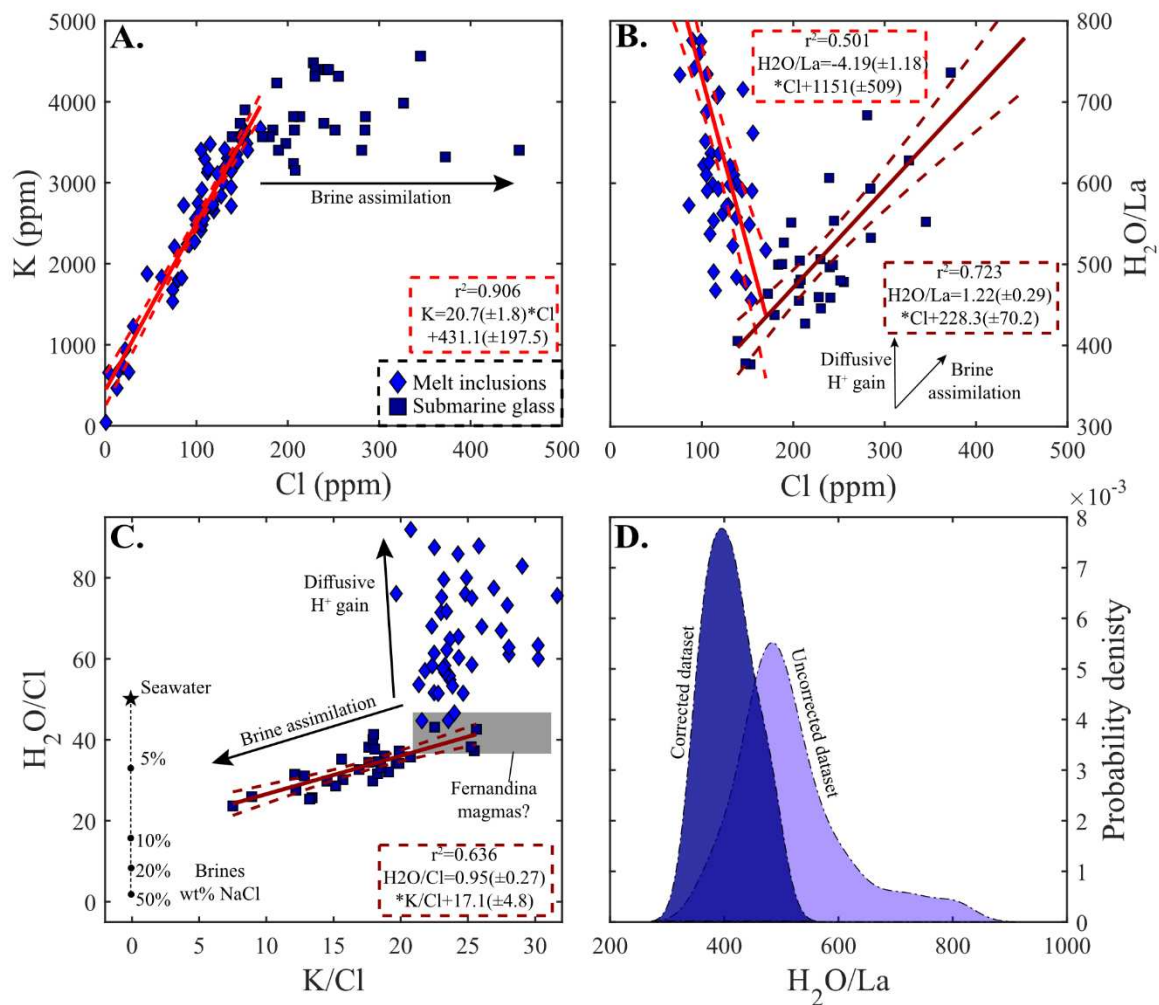
1252

1253 **Figure 8** – Summary of the content and evolution of volatiles in magmas from Floreana and  
 1254 Fernandina. Glass compositions, excluding the submarine glass analyses from Fernandina, and  
 1255 whole-rock compositions represent predicted H<sub>2</sub>O concentrations that are calculated using the La  
 1256 content measured in each sample and the H<sub>2</sub>O/La ratio that characterises the Fernandina and  
 1257 Floreana magmas. The values shown for the submarine glasses from Fernandina are the brine-  
 1258 corrected H<sub>2</sub>O contents. Density distributions on the right-hand axis show the distribution of  
 1259 predicted H<sub>2</sub>O concentrations for the Floreana whole-rocks (grey; Harpp et al., 2014) and for core  
 1260 pyroxene analyses (yellow; excluding crystals that show a chemical affinity to the gabbroic  
 1261 xenoliths). Black lines represent crystallisation models carried out in Petrolog v3.1.1.3  
 1262 (Danyushevsky and Plechov, 2011) to simulate how H<sub>2</sub>O would change during crystallisation of: (i)  
 1263 the most enriched; (ii) the average; and (iii) the most depleted compositions measured in the  
 1264 Fernandina melt inclusions (Peterson et al., 2017). Crystallisation models are carried out at ~300  
 1265 MPa and QFM, appropriate for western Galápagos volcanic systems (Stock et al., 2018). 2σ errors  
 1266 represent the fully propagated analytical precision for both H<sub>2</sub>O-rich and H<sub>2</sub>O-poor clinopyroxenes.  
 1267 Equilibrium melt Mg# is calculated for the clinopyroxenes using the formulation of Wood and Blundy  
 1268 (1997) assuming that the Fe<sup>3+</sup>/Fe<sub>tot</sub> ratio of the melt is ~0.15. Kernel density distribution bandwidths  
 1269 are calculated using the method of Sheather and Jones (1991).



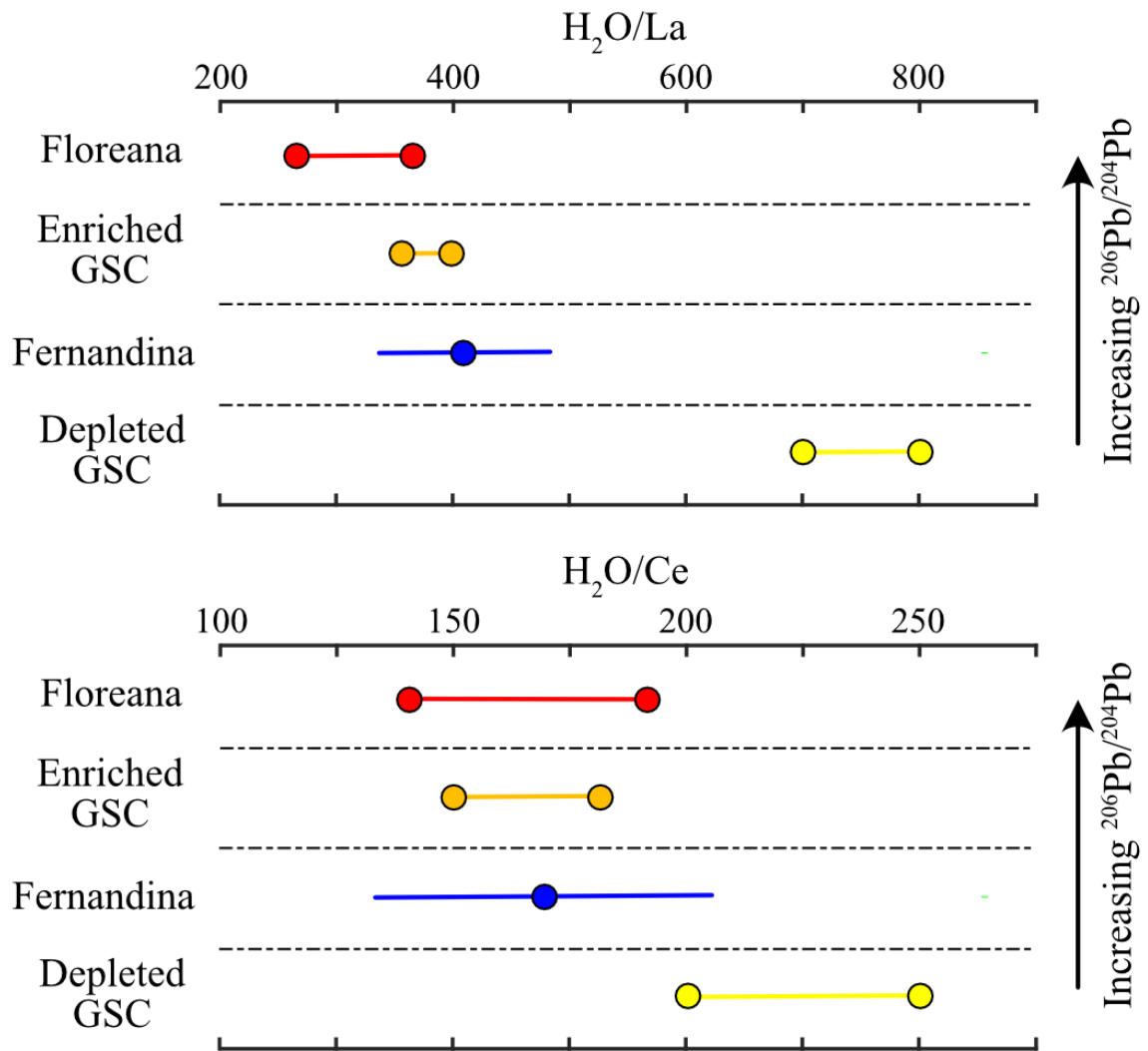
1270

1271 **Figure 9** – Pb isotope vs trace element systematics of the Floreana whole-rock (data from Harpp et  
 1272 al. 2014). In basalts with predicted  $H_2O$  contents  $< 0.8$  wt%, there is a statistically significant  
 1273 correlation (at the 99% confidence level) between the isotopic and trace element systematics of the  
 1274 Floreana basalts. However, those basalts with predicted  $H_2O$  contents  $> 0.8$  wt% do not follow this  
 1275 correlation and are isotopically indistinguishable from the rest of the Floreana basalts. Data from  
 1276 Harpp et al. (2014)



1277

1278 **Figure 10** – Insights into the volatile content of the Isla Fernandina basalts. **A.** There is a statistically  
 1279 significant correlation between K and Cl in the melt inclusion dataset of Koleszar et al. (2009), but  
 1280 the Cl concentrations measured in submarine glasses from Fernandina extend to much higher values  
 1281 at approximately constant K concentrations (Peterson et al., 2017). **B.** Diverging trends of Cl vs  
 1282 H<sub>2</sub>O/La are hypothesised to result from assimilation of a Cl-rich hydrothermal brine prior to eruption  
 1283 of the Fernandina basalts, and diffusive migration of H<sup>+</sup> between olivine-hosted melt inclusions and  
 1284 the carrier melt (incompatible trace element depleted melt inclusions from Koleszar et al. (2009) are  
 1285 excluded from the shown correlation). **C.** Evidence for assimilation of hydrothermal brines comes  
 1286 from the correlation between K/Cl and H<sub>2</sub>O/Cl. The intersection of this linear regression with the y-  
 1287 axis gives an estimate of the H<sub>2</sub>O/Cl content of the assimilated component. The grey regions in  
 1288 panels **B.** and **C.** display the hypothesised composition of primary Fernandina magmas. Estimated  
 1289 composition of the initial Fernandina magmas are shown in grey. **D.** Probability density distribution  
 1290 for H<sub>2</sub>O/La in the uncorrected (light blue) and brine-assimilation corrected (dark blue) submarine  
 1291 glass dataset. Dashed lines in **A., B., and C.** represent the 95% confidence limits on the various  
 1292 regression lines.



1293

1294 **Figure 11** – Summary of the H<sub>2</sub>O/REE systematics of basalts from different regions of the Galápagos  
 1295 Archipelago. The H<sub>2</sub>O/La ratios that characterise depleted and enriched basalts from the GSC are  
 1296 taken from Gleeson and Gibson (2021). In most cases the range of predicted H<sub>2</sub>O/La and H<sub>2</sub>O/Ce  
 1297 ratios are shown, with the circular symbols representing the maximum and minimum estimate. For  
 1298 Fernandina, however, the circle represents the mean of the brine-corrected H<sub>2</sub>O/La and H<sub>2</sub>O/Ce  
 1299 ratios in the Fernandina submarine basalts, with the solid line representing the 2σ deviation around  
 1300 this mean.